

# Integration of vacuum potential energy into ideal magnetohydrodynamic stability calculations for flux-core-spheromak configurations

F. Alladio,<sup>a)</sup> A. Mancuso, and P. Micozzi

Associazione EURATOM-ENEA sulla Fusione, CR Frascati, C.P. 65, 00044 Frascati, Rome, Italy

F. Rogier

ONERA-CERT/DTIM/M2SN 2, avenue Edouard Belin, Boîte Postale 4025-31055, Toulouse Cedex 4, France

(Received 8 February 2007; accepted 25 May 2007; published online 28 August 2007)

In the calculation of the ideal magnetohydrodynamic free-boundary stability of magnetoplasma equilibria, the integration of the perturbed magnetic energy in the vacuum region that can exist between the plasma edge and nearby conducting shells is extended to axisymmetric configurations composed in part by closed and in part by open field lines. Examples of such equilibria are flux-core-spheromaks and spherical tori with a plasma central column, where a magnetic separatrix divides a spherical torus—with closed field lines—from a central screw pinch discharge—with open field lines that end on the sustaining electrodes. These configurations pose two problems: their plasma-vacuum interface is composed of multiple flux surfaces (i.e., they enclose different values of toroidal and poloidal flux) and their plasma extends up to the symmetry axis. A Green's function method based on two-dimensional finite elements is used to solve both problems, and an application to the experimental results of the Tokyo University Spherical Torus No. 3 flux-core-spheromak experiment [N. Amemiya, A. Morita, and M. Katsurai, *J. Phys. Soc. Jpn.* **63**, 1552 (1993)] is illustrated. © 2007 American Institute of Physics. [DOI: 10.1063/1.2754632]

## I. INTRODUCTION

A great deal of care has been devoted to the calculation of the ideal magnetohydrodynamic (MHD) stability of magnetically confined plasma equilibria in the case that is usually more relevant to the analysis of experimental data, i.e., where conducting shells are present at a distance from the plasma-edge-free-boundary conditions.<sup>1</sup> However, most of the literature has been devoted to the case of doubly connected plasma toroids<sup>2–7</sup> (tokamaks, reverse field pinches, stellarators, etc.) endowed with closed flux surfaces; a few papers deal with the case of simple connected plasmas extending up to the symmetry axis<sup>8–10</sup> (spheromaks, field reversed configurations, etc.), whereas the case in which the confined plasma is composed of flux surfaces whose field lines are in part closed and in part open (ending on electrodes, as in flux-core spheromaks) has been treated only in the line-tying limit<sup>11</sup> and not in free-boundary conditions.

A recent Green's function method,<sup>12</sup> using one-dimensional finite elements (where the elements fill only the contours of the cross sections of the vacuum domain boundaries, i.e., the plasma-vacuum interface and the vacuum-ideal conducting shell boundary), was able to include in an effective way the treatment of simply connected shells around magnetically confined plasmas. The present paper starts from this Green's function method, but modifies it to a two-dimensional finite-element vacuum calculation, where the elements fill the whole cross section of the vacuum domain between the plasma edge and the ideal conducting shells. This simplifies the analytical treatment and allows for a natu-

ral extension to magnetic configurations whose field lines are partly closed and partly open.

The paper starts in Sec. II, detailing the two-dimensional (2D) finite-element vacuum method for doubly connected plasma configurations in the absence of X-points at the edge. Section III shows that, in the presence of regular X-points at the edge, the dominant errors in the perturbed plasma potential and in the perturbed vacuum magnetic energies compensate exactly. Section IV applies the 2D finite-element vacuum method to simply connected magnetic configurations, even in the presence of singular X-points on the symmetry axis. Section V extends the method to flux-core spheromaks, where multiple plasma-vacuum interfaces, and couplings that can exist among them, introduce some complications. Finally, Sec. VI applies the ideal MHD stability analysis to the results of the Tokyo University Spherical Torus No. 3 (TS-3) flux-core-spheromak (FCS) experiment, while Sec. VII contains a summary of the paper.

## II. PERTURBED VACUUM MAGNETIC ENERGY FOR DOUBLY CONNECTED PLASMA CONFIGURATIONS IN THE ABSENCE OF X-POINTS

Previous papers<sup>13</sup> have shown that the ideal magnetohydrodynamic (MHD) stability analysis of axisymmetric plasma equilibria is simplified if magnetic Boozer coordinates<sup>14</sup> ( $\psi_T$ -radial, i.e., toroidal flux divided by  $2\pi$ ,  $\theta$ -poloidal angle,  $\phi$ -toroidal angle with Jacobian  $\sqrt{g} \propto 1/B^2$ ), are used. For every (separable) toroidal mode number  $n$ , the perturbed plasma displacement  $\vec{\xi}$  is Fourier expanded in the poloidal angle, and the normal-mode equation<sup>15</sup>  $\delta W_p(\vec{\xi}^*, \vec{\xi}) = \omega^2 \delta W_k(\vec{\xi}^*, \vec{\xi})$  (where  $\delta W_p$  and  $\delta W_k$  are the perturbed potential and kinetic plasma energies and  $\omega^2$  is the eigenvalue) is

<sup>a)</sup>Electronic mail: alladio@frascati.enea.it

solved through a 1D radial finite-element method;  $\vec{\xi}$  is expressed<sup>16</sup> in terms of the normal  $\xi^\psi$ , binormal  $\eta^\psi$ , and parallel  $\mu$  displacement variables as follows:

$$\vec{\xi} = \xi^\psi \vec{e}_\psi + \eta^\psi \frac{\vec{B} \wedge \vec{\nabla} \psi_T}{B^2} + \left( \frac{I \eta^\psi}{B^2} - \mu \right) \vec{B}, \quad (1)$$

where  $\vec{e}_\psi$  is the Boozer covariant radial basis vector,<sup>17</sup>  $I(\psi_T) = \int \vec{\nabla} \wedge \vec{B} \cdot d\vec{S}_T / 2\pi$  is the normalized toroidal current and  $f(\psi_T) = \int \vec{\nabla} \wedge \vec{B} \cdot d\vec{S}_p / 2\pi$  is the normalized poloidal current. Whereas  $\xi^\psi$  is directly the Boozer normal contravariant component of  $\vec{\xi}$ ,  $\eta^\psi$  and  $\mu$  are defined in terms of the other contravariant components  $\xi^\theta$  and  $\xi^\phi$ :  $\xi^\psi = \vec{\xi} \cdot \vec{\nabla} \psi_T$ ,  $\eta^\psi = \vec{\xi} \cdot (\vec{\nabla} \theta - \mathcal{L} \vec{\nabla} \phi) = \xi^\theta - \mathcal{L} \xi^\phi$  and  $\mu = -\sqrt{g} \vec{\xi} \cdot \vec{\nabla} \phi = -\sqrt{g} \xi^\phi$ , where  $\mathcal{L}(\psi_T)$  is the rotational transform. In order to treat all the ideal MHD perturbations, including the ones with toroidal mode number  $n=0$ ,  $\vec{\xi}$  is better decomposed in terms of the normal  $\xi^\psi$ , binormal  $\eta^\psi$ , and parallel  $\bar{\mu}$  components (where  $\bar{\mu} = \mu - I \eta^\psi / B^2 - \beta_* \xi^\psi / B^2$ ), as follows:

$$\vec{\xi} = \xi^\psi \frac{\vec{\nabla} \psi_T}{|\vec{\nabla} \psi_T|^2} + (\eta^\psi - \gamma_* \xi^\psi) \frac{\vec{B} \wedge \vec{\nabla} \psi_T}{B^2} - \bar{\mu} \vec{B}, \quad (2)$$

where  $\beta_*(\psi_T, \theta)$  is the nonorthogonality coefficient,<sup>14</sup> defined by the covariant representation of the magnetic field  $\vec{B} = \beta_* \vec{\nabla} \psi_T + I \vec{\nabla} \theta + f \vec{\nabla} \phi$  and  $\gamma_*(\psi_T, \theta) = \vec{\nabla} \psi_T \cdot (\vec{\nabla} \theta - \mathcal{L} \vec{\nabla} \phi) / |\vec{\nabla} \psi_T|^2$  is the ‘‘integrated residual shear.’’<sup>18</sup>

In the calculation of the ideal MHD stability, the numerical normal-mode equation

$$\vec{W} \cdot |\vec{x}\rangle = \omega^2 \vec{K} \cdot |\vec{x}\rangle \quad (3)$$

must be discretized over the radial mesh points  $\psi_T^j$ ,  $j = 0, 1, \dots, N_\psi$  and solved, finding the eigenfunction  $|\vec{x}\rangle \equiv (\xi_l^j, \eta_l^j, \mu_l^j)$  with the minimum eigenvalue  $\omega^2$ ; the numerically discretized potential energy matrix  $\vec{W}$  and the kinetic energy matrix  $\vec{K}$  (positive definite) are symmetric and block-diagonal. The radial behavior of  $\xi_l(\psi_T)$ ,  $\eta_l(\psi_T)$ ,  $\mu_l(\psi_T)$ , and  $\partial \xi_l / \partial \psi_T$  is approximated by a one-dimensional finite-element method.<sup>19,20</sup> Details about the mesh resolution that is needed for the code to give reliably accurate calculations are given in Sec. IV. The simplest boundary condition is the fixed-boundary condition  $\xi^\psi(\psi_T^{\text{edge}}) = 0$ , which can be directly enforced into (3) and corresponds to a perfectly conducting shell in contact with the plasma edge. More interesting and more relevant to the analysis of experimental data is the free-boundary condition, where conducting shells can be placed at a distance from the plasma edge, which is therefore free to move, i.e.,  $\xi^\psi(\psi_T^{\text{edge}}) \neq 0$ . The normal-mode equation (3) is modified by the free-boundary vacuum magnetic energy through an additional term,<sup>1,12</sup>  $\delta W_v$ , present only upon the last ( $j = N_\psi$ ) radial mesh point  $\psi_T^{N_\psi}$ :

$$\delta W_p(\vec{\xi}^*, \vec{\xi}) + \delta W_v[\xi^{\psi*}(\psi_T^{N_\psi}) \xi^\psi(\psi_T^{N_\psi})] = \omega^2 \delta W_k(\vec{\xi}^*, \vec{\xi}). \quad (4)$$

The STABLE code<sup>20</sup> solves the eigenvalue problem (4) by an inverse iteration method, which finds all the lowest discrete eigenvalues and the corresponding eigenvectors. For the treatment of the magnetic energy in the vacuum region sur-

rounding a free-boundary axisymmetric plasma, this paper follows the Green’s function method.<sup>4</sup> However, the sophisticated treatment of the Green’s function, which is required by the use of a 1D finite-element method (where the elements fill only the contours of the cross section of the vacuum domain boundaries, i.e., the plasma-vacuum interface and the vacuum-ideal conducting shell boundary<sup>12</sup>), is dispensed with in the present paper: its burden is instead shifted to a 2D finite-element method, where the elements fill the whole cross section of the vacuum domain. The results of this section, although detailed in terms of the Boozer coordinates, apply in general to any straight field line coordinate system (i.e., with  $\theta_{\text{magn}} - \mathcal{L} \phi_{\text{magn}} = \text{const}$  along magnetic field lines), with radial coordinate  $\psi_{\text{magn}}$ , poloidal and toroidal angles  $\theta_{\text{magn}}$  and  $\phi_{\text{magn}}$ , deviation from geometric azimuth  $\nu_{\text{magn}}(\theta_{\text{magn}}) = \phi_{\text{magn}} - \varphi$ , and Jacobian  $\sqrt{g_{\text{magn}}}$ , simply replacing the equivalent Boozer quantities  $\psi_T$ ,  $\theta$ ,  $\phi$ ,  $\nu$ , and  $\sqrt{g}$ .

In this section, it will be assumed that a doubly connected toroidal plasma-vacuum interface [ $\psi_T = \psi_T^{\text{edge}}$ , with a nonvanishing rotational transform  $\mathcal{L}^{\text{edge}} = \mathcal{L}(\psi_T^{\text{edge}}) \neq 0$ ], describes the plasma edge surface. The perturbed vacuum magnetic energy  $\delta W_v$  is expressed as a function of the perturbed scalar magnetic potential  $\Phi$ :

$$\delta W_v = \frac{\mu_0}{2} \oint \oint_{S_\psi} \Phi \vec{\nabla} \Phi \cdot d\vec{S}_\psi, \quad (5)$$

where the definition of  $\Phi$ , in terms of the perturbed field  $\vec{B}_1$ , is

$$\vec{B}_1 = -\mu_0 \vec{\nabla} \Phi \quad (6)$$

and the differential surface element of the plasma-vacuum interface is

$$d\vec{S}_\psi = -\sqrt{g} \vec{\nabla} \psi_T d\theta d\phi|_{\psi_T^{\text{edge}}}. \quad (7)$$

$\Phi$  has to be calculated in the vacuum region, taking into account the appropriate boundary condition at the plasma-vacuum interface,

$$\mu_0 \vec{\nabla} \Phi|_{\psi_T^{\text{edge}}} \cdot d\vec{S}_\psi = -\vec{\nabla} \wedge (\vec{\nabla} \wedge \vec{B})|_{\psi_T^{\text{edge}}} \cdot d\vec{S}_\psi, \quad (8)$$

and the boundary conditions on the axisymmetric ideal conducting shells  $S_c$  (which can either surround or not surround the plasma),

$$\vec{\nabla} \Phi \cdot d\vec{S}_c = 0. \quad (9)$$

Both surface elements  $d\vec{S}_\psi$  and  $d\vec{S}_c$  are oriented out from the vacuum region. For a given toroidal mode number  $n$ , the 2D quantities  $\tilde{\Phi}^{nc}$  and  $\tilde{\Phi}^{ns}$  are defined over the cross section of the whole vacuum region,

$$\Phi = \tilde{\Phi}^{nc} \cos(n\varphi) + \tilde{\Phi}^{ns} \sin(n\varphi), \quad (10)$$

in terms of the geometrical azimuth  $\varphi$ . The contour quantities  $\tilde{B}^{nc}$  and  $\tilde{B}^{ns}$ ,

$$\begin{aligned}\tilde{B}^{nc} &= \mu_0 \sqrt{g} \frac{\partial \tilde{\Phi}^{nc}}{\partial n} \bigg|_{\psi_T^{\text{edge}}} \bigg|_{\vec{\nabla} \psi_T}, \\ \tilde{B}^{ns} &= \mu_0 \sqrt{g} \frac{\partial \tilde{\Phi}^{ns}}{\partial n} \bigg|_{\psi_T^{\text{edge}}} \bigg|_{\vec{\nabla} \psi_T},\end{aligned}\quad (11)$$

are instead introduced only upon the poloidal contour of the plasma edge cross section; here  $(\partial/\partial n)$  means the normal derivative at the ideal conducting shells or at the plasma-vacuum interface, in this latter case being along the unitary vector  $\hat{n}^{\text{edge}} = -\vec{\nabla} \psi_T / |\vec{\nabla} \psi_T|_{\psi_T^{\text{edge}}}$ . The quantities (10) and (11) define  $\delta W_v$  as an integral over the poloidal contour  $l_\psi$  of the cross section of the plasma-vacuum interface, using (7) for the surface element and integrating over the azimuth  $\varphi$ ,

$$\delta W_v = \frac{\pi}{2} \oint_{l_\psi} [\tilde{\Phi}^{nc} \tilde{B}^{nc} + \tilde{\Phi}^{ns} \tilde{B}^{ns}] d\theta. \quad (12)$$

From the continuity link (8) between  $\Phi$  and  $\xi$ , one gets

$$\frac{\partial \Phi}{\partial n} \bigg|_{s_\psi} = \frac{1}{\mu_0 \sqrt{g} |\vec{\nabla} \psi_T|} \left[ \iota \frac{\partial \xi^\psi}{\partial \theta} + \frac{\partial \xi^\psi}{\partial \phi} \right] \bigg|_{\psi_T^{\text{edge}}}, \quad (13)$$

i.e.,  $\delta W_v$  is a quadratic form of the radial perturbed displacement variable at the plasma-vacuum interface,

$$\xi_{\text{edge}}^\psi = \vec{\xi} \cdot \vec{\nabla} \psi_T |_{\psi_T^{\text{edge}}}. \quad (14)$$

Substituting into (13) the Fourier expansion of the normal displacement variable  $\xi_{\text{edge}}^\psi = \sum_l \xi_l(\psi_T^{\text{edge}}) \sin(m_l \theta^{\text{edge}} - n \phi^{\text{edge}})$ , where  $m_l$  are the poloidal mode numbers of the perturbation, the dependence upon the Boozer poloidal angles  $\theta^{\text{edge}}$  and  $\phi^{\text{edge}}$  at the plasma-vacuum interface is put in evidence,

$$\begin{aligned}\frac{\partial \Phi}{\partial n} (\theta^{\text{edge}}) \bigg|_{s_\psi} &= \frac{1}{\mu_0 \sqrt{g}(\theta^{\text{edge}}) |\vec{\nabla} \psi_T|_{\theta^{\text{edge}}}} \sum_l (\iota^{\text{edge}} m_l - n) \\ &\times \xi_l(\psi_T^{\text{edge}}) \cos(m_l \theta^{\text{edge}} - n \phi^{\text{edge}}).\end{aligned}\quad (15)$$

The reduction to a sine component for  $\xi^\psi$  and to a cosine component for  $\eta^\psi$  and  $\mu$  is permitted if up-down symmetric equilibria are assumed (as in this paper); in general sine and cosine components for all the displacement variables should be included. The choice of the angular dependence ( $m_l \theta - n \phi$ ) is in accordance with the choice of directions for the Boozer coordinates<sup>14</sup> and corresponds to the requirement of accounting for the most unstable modes [the ones with wave vector  $\vec{k}$  such that  $\vec{k} \cdot \vec{B} \approx 0$ , or  $\iota(\psi_T) m_l - n \approx 0$ ] with positive mode numbers  $m_l$  and  $n$ . However, the vacuum analysis has been performed using the geometrical azimuth  $\varphi$ , whereas the perturbed potential plasma energy is expressed through the toroidal Boozer angle  $\phi = \varphi + \nu(\theta)$ , with<sup>17</sup>  $\nu(\theta) = -\sum_{p=0}^{40} \delta_p^\nu(\psi_T) \cos(-p\theta + \lambda_p^\nu)$ . Therefore,

$$\begin{aligned}\frac{\partial \tilde{\Phi}^{nc}}{\partial n} (\theta^{\text{edge}}) \bigg|_{s_\psi} &= \frac{\sum_l (\iota^{\text{edge}} m_l - n) \xi_l(\psi_T^{\text{edge}}) \cos[m_l \theta^{\text{edge}} - n \nu(\theta^{\text{edge}})]}{\mu_0 \sqrt{g}(\theta^{\text{edge}}) |\vec{\nabla} \psi_T|_{\theta^{\text{edge}}}},\end{aligned}\quad (16)$$

$$\begin{aligned}\frac{\partial \tilde{\Phi}^{ns}}{\partial n} (\theta^{\text{edge}}) \bigg|_{s_\psi} &= \frac{\sum_l (\iota^{\text{edge}} m_l - n) \xi_l(\psi_T^{\text{edge}}) \sin[m_l \theta^{\text{edge}} - n \nu(\theta^{\text{edge}})]}{\mu_0 \sqrt{g}(\theta^{\text{edge}}) |\vec{\nabla} \psi_T|_{\theta^{\text{edge}}}}\end{aligned}\quad (17)$$

or

$$\tilde{B}^{nc}(\theta^{\text{edge}}) = \sum_l (\iota^{\text{edge}} m_l - n) \xi_l(\psi_T^{\text{edge}}) \cos[m_l \theta^{\text{edge}} - n \nu(\theta^{\text{edge}})], \quad (18)$$

$$\tilde{B}^{ns}(\theta^{\text{edge}}) = \sum_l (\iota^{\text{edge}} m_l - n) \xi_l(\psi_T^{\text{edge}}) \sin[m_l \theta^{\text{edge}} - n \nu(\theta^{\text{edge}})]. \quad (19)$$

The vacuum energy  $\delta W_v$  (12) becomes the Fourier series,

$$\begin{aligned}\delta W_v &= \frac{\pi}{2} \sum_l (\iota^{\text{edge}} m_l - n) \xi_l(\psi_T^{\text{edge}}) \\ &\times \oint_{l_\psi} [\tilde{\Phi}^{nc}(\theta^{\text{edge}}) \cos[m_l \theta^{\text{edge}} - n \nu(\theta^{\text{edge}})] \\ &+ \tilde{\Phi}^{ns}(\theta^{\text{edge}}) \sin[m_l \theta^{\text{edge}} - n \nu(\theta^{\text{edge}})]] d\theta^{\text{edge}}.\end{aligned}\quad (20)$$

The Laplace equation obeyed by the 2D scalar potentials  $\tilde{\Phi}^{nc}$  and  $\tilde{\Phi}^{ns}$  in the vacuum region is, in cylindrical coordinates  $(R, \varphi, Z)$ ,

$$\frac{1}{R} \frac{\partial}{\partial R} \left( R \frac{\partial \tilde{\Phi}^n \Big|_s^c}{\partial R} \right) + \frac{\partial^2 \tilde{\Phi}^n \Big|_s^c}{\partial Z^2} - \frac{n^2}{R^2} \tilde{\Phi}^n \Big|_s^c = 0, \quad (21)$$

with boundary conditions (9) on the ideal conducting shells:

$$\frac{\partial \tilde{\Phi}^n \Big|_s^c}{\partial n} \bigg|_{s_c} = 0, \quad (22)$$

and with the boundary conditions (16) and (17) rewritten in terms of the ‘‘source’’ Boozer poloidal angle  $\theta'$  on the plasma-vacuum interface. Equation (21) is solved by a 2D finite-elements method in the vacuum region; more information about this method is provided in Appendix A. The solutions, restricted upon the plasma-vacuum interface, are expressed as a function of the poloidal ‘‘observation’’ angle  $\theta^{\text{edge}}$ ,

$$\tilde{\Phi}^{nc}(\theta^{\text{edge}})|_{S_\psi} = \sum_k \frac{\xi_k(\psi_T^{\text{edge}})(\mathcal{L}^{\text{edge}} m_k - n)}{\mu_0} \times F_k^c \left( \theta^{\text{edge}}, \frac{\cos[m_k \theta' - n\nu(\theta')]}{\sqrt{g(\theta')} |\vec{\nabla} \psi_T|_{\theta'}} \right) \quad (23)$$

and

$$\tilde{\Phi}^{ns}(\theta^{\text{edge}})|_{S_\psi} = \sum_k \frac{\xi_k(\psi_T^{\text{edge}})(\mathcal{L}^{\text{edge}} m_k - n)}{\mu_0} \times F_k^s \left( \theta^{\text{edge}}, \frac{\sin[m_k \theta' - n\nu(\theta')]}{\sqrt{g(\theta')} |\vec{\nabla} \psi_T|_{\theta'}} \right), \quad (24)$$

where  $\theta'$  is the “source” poloidal angle (again upon the plasma-vacuum interface) and  $F_k^c$  and  $F_k^s$  act as reduced Green’s functions, whose definitions are Eqs. (23) and (24); their actual evaluations are given in Eqs. (A8) and (A9) in Appendix A. The perturbed vacuum magnetic energy (20) is then integrated in the energy principle (4):

$$\delta W_v = \frac{1}{2\mu_0} \sum_{l,k} \{[\xi_l(\psi_T^{\text{edge}})]\{R_{lk}[\xi_k(\psi_T^{\text{edge}})]\}, \quad (25)$$

with the coefficients  $R_{lk}$  of the vacuum energy matrix defined as

$$R_{lk} = \pi \oint_{l_\psi} d\theta^{\text{edge}} [(\mathcal{L}^{\text{edge}} m_l - n) \cos[m_l \theta^{\text{edge}} - n\nu(\theta^{\text{edge}})]] \times F_k^c \left( \theta^{\text{edge}}, \frac{(\mathcal{L}^{\text{edge}} m_k - n) \cos[m_k \theta' - n\nu(\theta')]}{\sqrt{g(\theta')} |\vec{\nabla} \psi_T|_{\theta'}} \right) + \pi \oint_{l_\psi} d\theta^{\text{edge}} [(\mathcal{L}^{\text{edge}} m_l - n) \sin[m_l \theta^{\text{edge}} - n\nu(\theta^{\text{edge}})]] \times F_k^s \left( \theta^{\text{edge}}, \frac{(\mathcal{L}^{\text{edge}} m_k - n) \sin[m_k \theta' - n\nu(\theta')]}{\sqrt{g(\theta')} |\vec{\nabla} \psi_T|_{\theta'}} \right). \quad (26)$$

The definition of  $R_{lk}$  is different from Ref. 12: the resonant  $(\mathcal{L}^{\text{edge}} m_l - n)$  terms are included inside the coefficients, as they must be in the case of the plasma-vacuum interfaces composed by multiple flux surfaces (see Sec. V). The results of the STABLE code<sup>20</sup>—including the effect of vacuum term—is checked in Appendix B against the (well known) ideal MHD stability<sup>21</sup> of the analytic Solovév equilibria.<sup>22</sup>

### III. PERTURBED VACUUM MAGNETIC ENERGY FOR DOUBLY CONNECTED PLASMA CONFIGURATIONS IN THE PRESENCE OF REGULAR X-POINTS

In the case of a doubly connected plasma equilibrium not limited by a magnetic separatrix, the last radial mesh point ( $j=N_\psi$ ) for the stability calculation coincides with the plasma-vacuum interface,  $\psi_T^N = \psi_T^{\text{edge}}$ . If instead the doubly connected plasma-vacuum interface is a magnetic separatrix with regular X-points [ $\psi_T = \psi_T^X$ ,  $\vec{B} \neq 0$ , and  $\mathcal{L}(\psi_T^X) = 0$ ], an intensified numerical radial mesh can be set up: various divergences<sup>17</sup> compel us to stop the calculation of the Boozer coordinates and of the perturbed plasma energy at a distance

from the magnetic separatrix where  $\mathcal{L}(\psi_T)$  can still be calculated numerically—typically  $j=N_\psi$  at  $\psi_T^N = \psi_T^X - \varepsilon_{\text{ST}}$ , with  $\varepsilon_{\text{ST}} \approx (10^{-3} - 10^{-2}) \cdot |\psi_T^X|$ . Although the general result that has been obtained for unstable free-boundary modes is that the growth rate decreases as the last mesh point approaches the magnetic separatrix,<sup>20,23</sup> one should ask whether the behavior<sup>17</sup> of  $|\vec{\nabla} \psi_T|$ , which vanishes near the X-point like  $\sqrt{|\psi_T^X - \psi_T|} |\ln |\psi_T^X - \psi_T||$  and diverges far from the X-point like  $|\ln |\psi_T^X - \psi_T||$ , can introduce problems of divergence in the vacuum energy term. If no surface equilibrium plasma current flows at the plasma-vacuum interface, the radial derivatives of the perturbed potential plasma energy  $\delta W_p$  and of the free-boundary vacuum perturbed magnetic energy  $\delta W_v$  (25) are opposite,

$$\lim_{\psi_T^N \rightarrow \psi_T^X} [\partial(\delta W_v + \delta W_p)/\partial \psi_T]_{\psi_T^N} = 0. \quad (27)$$

So the choice of the exact position ( $\psi_T^N = \psi_T^X - \varepsilon_{\text{ST}}$ ) of the last magnetic surface ( $j=N_\psi$ ) for the stability calculation does not seem particularly critical, as the dominant errors in the plasma and in the vacuum magnetic energies compensate exactly. On the other hand, numerical problems associated with the singularity of the Boozer coordinates still remain, in particular the need to include Fourier components with large poloidal numbers  $m_l$ . The demonstration of (27) is based on the division of the incompressible plasma energy  $\delta W_p^i$  in two parts. The first part is due to the perturbed field within the plasma,<sup>20</sup>

$$\delta W_p^{i,\vec{\nabla} \wedge (\vec{\xi} \wedge \vec{B})} = \frac{1}{2} \int \int \int_{V_p} dV \left[ \frac{|\vec{\nabla} \wedge (\vec{\xi} \wedge \vec{B})|^2}{\mu_0} \right], \quad (28)$$

the second part<sup>20</sup> contains the instability driving terms, i.e., the parallel current density  $(\vec{j} \cdot \vec{B})/B^2$  and the pressure gradient  $d\rho(\psi_T)/d\psi_T$ :

$$\delta W_p^{i,\vec{\nabla} p \cdot \vec{j} \cdot \vec{B}} = \delta W_p^i - \delta W_p^{i,\vec{\nabla} \wedge (\vec{\xi} \wedge \vec{B})}. \quad (29)$$

The “perturbed field part”  $\delta W_p^{i,\vec{\nabla} \wedge (\vec{\xi} \wedge \vec{B})}$  contains terms that can be sources of divergence; the “plasma part”  $\delta W_p^{i,\vec{\nabla} p \cdot \vec{j} \cdot \vec{B}}$  does not contain any of them. But if no surface plasma current flows upon the plasma-vacuum interface, the continuity condition between the vacuum field  $-\mu_0 \vec{\nabla} \Phi|_{\psi_T^X}$  and the plasma field  $\vec{\nabla} \wedge (\vec{\xi} \wedge \vec{B})|_{\psi_T^X}$  makes the derivative of the vacuum magnetic energy and of the overall perturbed field part, with respect to the choice of  $\varepsilon_{\text{ST}}$ , just equal and opposite,

$$\lim_{\psi_T^N \rightarrow \psi_T^X} \frac{\partial}{\partial \psi_T} (2\delta W_v) \Big|_{\psi_T^N} = - \lim_{\psi_T^N \rightarrow \psi_T^X} \frac{\partial}{\partial \psi_T} (2\delta W_p^{i,\vec{\nabla} \wedge (\vec{\xi} \wedge \vec{B})})_{\psi_T^N}. \quad (30)$$

For the compressible kinetic plasma energy  $\delta W_k$ , the most dangerous term near the edge magnetic separatrix<sup>20</sup> is  $\int_{\psi_T^X}^{\psi_T} d\psi_T \rho_0(\psi_T) \int_{\theta_{\min}}^{\theta_{\max}} d\theta \sqrt{g} (1/|\vec{\nabla} \psi_T|^2 + \gamma^2 |\vec{\nabla} \psi_T|^2/B^2) (\xi^\psi)^2$ , which, accounting for the regular behavior of  $\xi^\psi$  at the magnetic separatrix, produces the convergent integral,  $\int_{\psi_T^X}^{\psi_T} d\psi_T \rho_0(\psi_T) / |\ln |\psi_T^X - \psi_T||^2$ . The compressible plasma mag-

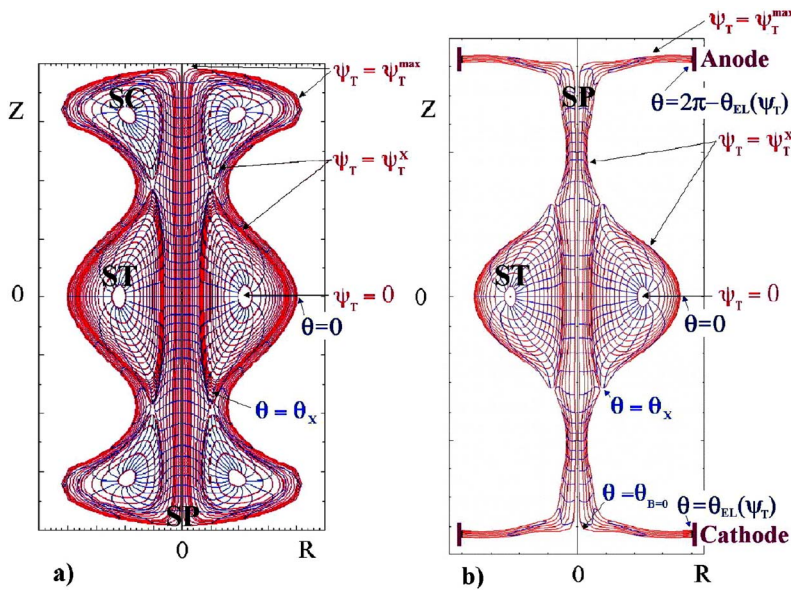


FIG. 1. (Color online) Magnetic coordinates cross section for (a) a CKF configuration, composed of ST, SP, and two SC, showing the origin  $\theta=0$  and the “separatrix” angle  $\theta=\theta_x$  that labels the lower regular X-point, (b) a FCS configuration, composed of ST and SP, showing the angles  $\theta_{B=0}$  labeling the lower singular X-point,  $\theta_x$  labeling the lower regular X-point, and  $\theta_{EL}(\psi_T)$  that marks the position of the lower plasma-electrode interface.

netic energy  $\delta W_p = (\Gamma/2) \int_0^{\psi_T^x} d\psi_T p(\psi_T) \int_{\theta_{\min}}^{\theta_{\max}} d\theta \int_0^{2\pi} (\vec{\nabla} \cdot \vec{\xi})^2 d\phi$  does not exhibit any divergence; as a matter of fact, the equation of motion<sup>15</sup>  $-\rho_0 \omega^2 \vec{\xi} = -\vec{\nabla} p_1 + (\vec{\nabla} \wedge \vec{B}) \wedge \vec{B}_1 / \mu_0 + (\vec{\nabla} \wedge \vec{B}_1) \wedge \vec{B} / \mu_0$ , with  $\vec{B}_1 = \vec{\nabla} \wedge (\vec{\xi} \wedge \vec{B})$  and  $p_1 = -\vec{\xi} \cdot \vec{\nabla} p - \Gamma p \vec{\nabla} \cdot \vec{\xi}$ , dotted with  $\vec{B}$ , gives  $-\rho_0 \omega^2 \vec{B} \cdot \vec{\xi} = \Gamma p (\vec{B} \cdot \vec{\nabla}) (\vec{\nabla} \cdot \vec{\xi})$ . Upon the magnetic separatrix ( $l=0$ ), the asymptotic behavior of  $(\vec{\nabla} \cdot \vec{\xi})$  is therefore the same as that of  $(\vec{B} \cdot \vec{\xi})$ , which means<sup>20</sup>  $O(1/|\ln|\psi_T^x - \psi_T|)| \leq \lim_{\psi_T \rightarrow \psi_T^x} (\vec{\nabla} \cdot \vec{\xi}) \leq O(1)$ .

#### IV. PERTURBED VACUUM MAGNETIC ENERGY FOR SIMPLY CONNECTED PLASMA CONFIGURATIONS IN THE PRESENCE OF SINGULAR X-POINTS

An analytical treatment, similar to the one detailed above, can be repeated step by step (with the obvious changes when the terms most at risk of divergence must be considered) and gives a result strictly similar to (27) for an edge magnetic separatrix with singular X-points [ $\psi_T = \psi_T^{\max}$ ,  $\vec{B}=0$ , and  $l(\psi_T^{\max}) \neq 0$ ], which is the plasma-vacuum interface of a simply connected plasma equilibrium, as in the case of CKF and FCS configurations (see Fig. 1).

An example of the Chandrasekhar-Kendall-Furth (CKF)<sup>24</sup> system is shown in Fig. 1(a). It is composed of a main spherical torus (ST, carrying a current with a main toroidal component  $I_{ST}$ ); two secondary tori (SC, each carrying a current with a main toroidal component  $I_{SC}$ ) connected to the main torus by regular X-points ( $\vec{B} \neq 0$ ); and an outermost toroidal shell plasma (SP, carrying a current with a main poloidal component  $I_e$ ) that extends up to the symmetry axis ( $R=0$ ), where it forms singular X-points ( $\vec{B}=0$ ) and surrounds the three tori.

An example of the FCS configuration<sup>25</sup> or spherical torus with plasma central column<sup>26</sup> (ST-PCC) is shown in Fig. 1(b). It refers to the PROTO-SPHERA experiment,<sup>27</sup> which is under construction in CR-ENEA Frascati. In PROTO-SPHERA, an embedded magnetic separatrix divides

a spherical torus, which has closed flux surfaces and carries a total toroidal current  $I_{ST}$ , from a screw pinch (SP) discharge, which has open flux surfaces ending upon electrodes and carries a (mainly poloidal) plasma electrode current  $I_e$ . The SP discharge takes the shape of a disk in front of both annular electrodes; both electrodes, on top and bottom of the machine, can therefore be hosted in two chambers separated, as much as possible, from the main chamber containing the spherical torus. Figure 1 shows also the ordering<sup>17</sup> of the radial variable  $\psi_T$  for these simply connected configurations, along with the values of the Boozer poloidal angle that label the different types of X-points ( $\theta_x$  for the lower ordinary one,  $\theta_{B=0}$  for the lower singular one) and the electrode-plasma interface [ $\theta_{EL}(\psi_T)$  for the lower annular electrode, with  $\psi_T^x \leq \psi_T \leq \psi_T^{\max}$ ].

The radial mesh of a numerical run for a CKF configuration is typically composed of 140 radial points: 70 inside the ST, 30 of which concentrated near the separatrix; 40 inside the SP, 20 of which concentrated near the separatrix; and 30 in either of the two up/down symmetric SCs. For both FCS as well as for CKF configurations, acceptable convergence of the most unstable eigenvalue is obtained only if the distance between the magnetic separatrix and the last mesh point is less than  $\varepsilon_{ST} = |\psi_T^x - \psi_T| < 2.5 \times 10^{-2} \cdot \psi_T^x$ . The study of convergence of the most unstable eigenvalue, illustrated in Ref. 20, shows that the choice of  $m_l = [-5, 15]$  is reasonable.

The compressible plasma potential energy  $\delta W_p^c$  is reduced to convergent integrals, even if near the singular X-points<sup>17</sup>  $\lim_{\psi_T \rightarrow \psi_T^{\max}, \theta \rightarrow \theta_{B=0}} (\vec{\nabla} \cdot \vec{\xi}) < O(1/r)$ , and the compressible kinetic plasma energy  $\delta W_k$  is also reduced to convergent integrals by the asymptotic behavior of the parallel displacement variable<sup>20</sup>  $\vec{\mu}$ . However, the decomposition (2) for the perturbed plasma displacement  $\vec{\xi}$  is not the best one if the plasma extends, like in PROTO-SPHERA, up to the symmetry axis ( $R=0, \psi_T = \psi_T^{\max}$ ); as a matter of fact,  $\lim_{R \rightarrow 0} |\vec{\nabla} \psi_T| \propto R$ , therefore the regularity condition  $\xi^\psi(\psi_T^{\max}) = 0$  should be imposed in the stability solution if this

condition is not already enforced by the behavior of the metrics coefficients on a radial mesh sufficiently refined near  $R=0$ . However, on top and bottom of the configuration, after the degenerate X-point, the flux surface  $\psi_T = \psi_T^{\max}$  does not coincide anymore with the symmetry axis, therefore the regularity condition  $\xi^\psi(\psi_T^{\max})=0$  should not be imposed<sup>20</sup> in any free-boundary [i.e.,  $\xi(\psi_T^{\max}, \theta, \phi) \neq 0$ ] ideal MHD stability calculation.

In general, a change of variable for the radial displacement,

$$\xi^\psi = \xi R^N, \quad (31)$$

with  $N \geq 1$ , is able to decouple the symmetry axis ( $R=0$ ) from the plasma edge ( $R \neq 0$ ). The choice of the exponent  $N$ , to be used in (31), is determined by the requirement that the incompressible plasma magnetic energy does not diverge.

The term most at risk is<sup>20</sup>  $\delta W_p^i = \int_0^{\psi_T^{\max}} d\psi_T \int_0^{2\pi} d\phi \times \int_{\theta_{\min}}^{\theta_{\max}} d\theta \{ \dots \sqrt{g} B^2 N^2 R^{2N-2} (\partial R / \partial \psi_T)^2 (\xi)^2 \dots \} 2\mu_0$ ; near  $R=0$ ,

it becomes  $\delta W_p^i \propto \int_0^R dR \{ \dots R R^{2N-2} (1/R)^2 (\xi)^2 \dots \}$ , therefore, even for  $\lim_{R \rightarrow 0} \xi = \text{const}$ , the smallest integer exponent that avoids divergences is  $N=2$ . Furthermore, at the singular X-point ( $\vec{B}=0$ ), there is the prescription<sup>20</sup> that  $\eta^\psi(\psi_T \rightarrow \psi_T^{\max}) \leq o(r^{1/2})$ , where  $r$  is the local distance from the X-point. So the condition  $\eta^\psi(\psi_T^{\max})=0$  should be imposed in the stability solution, but it cannot, as no radial derivative of the binormal displacement  $\partial \eta^\psi / \partial \psi_T$  appears in the energy principle. The solution is to change also the binormal displacement variable,

$$\eta^\psi = \eta B. \quad (32)$$

In terms of the new  $(\xi, \eta, \bar{\mu})$  variables,  $\vec{\xi}$  becomes

$$\vec{\xi} = \xi R^N \frac{\vec{\nabla} \psi_T}{|\vec{\nabla} \psi_T|^2} + (\eta B - \gamma_* R^N \xi) \frac{\vec{B} \wedge \vec{\nabla} \psi_T}{B^2} - \bar{\mu} \vec{B}. \quad (33)$$

The boundary conditions (16) and (17) become

$$\left. \frac{\partial \tilde{\Phi}^{nc}}{\partial n}(\theta^{(i)}) \right|_{S_\psi^{v(i)}} = \frac{\sum_k \left[ (\ell^{v(i)} m_k - n) [R(\theta^{(i)})]^N \cos[m_k \theta^{v(i)} - n \nu(\theta^{(i)})] + \ell^{v(i)} N [R(\theta^{(i)})]^{N-1} \left( \frac{\partial R}{\partial \theta} \right) \sin[m_k \theta^{v(i)} - n \nu(\theta^{(i)})] \right]}{\mu_0 \sqrt{g(\theta^{(i)})} |\vec{\nabla} \psi_T|_{\theta^{(i)}}} \times \xi_k(\psi_T^{v(i)}), \quad (34)$$

$$\left. \frac{\partial \tilde{\Phi}^{ns}}{\partial n}(\theta^{(i)}) \right|_{S_\psi^{v(i)}} = \frac{\sum_k \left[ (\ell^{v(i)} m_k - n) [R(\theta^{(i)})]^N \sin[m_k \theta^{v(i)} - n \nu(\theta^{(i)})] - \ell^{v(i)} N [R(\theta^{(i)})]^{N-1} \left( \frac{\partial R}{\partial \theta} \right) \cos[m_k \theta^{v(i)} - n \nu(\theta^{(i)})] \right]}{\mu_0 \sqrt{g(\theta^{(i)})} |\vec{\nabla} \psi_T|_{\theta^{(i)}}} \times \xi_k(\psi_T^{v(i)}), \quad (35)$$

on each of the  $\psi_T^{v(i)}$  plasma-vacuum interfaces (if there are many, like in the cases of FCS configurations), where  $(\partial/\partial n)$  means the normal derivative, along the unitary vector  $\hat{n}^{v(i)} = -\vec{\nabla} \psi_T|_{\theta^{(i)}} / |\vec{\nabla} \psi_T|_{\theta^{(i)}}$ . Starting from Eqs. (34) and (35) and for the remainder of this paper,  $\xi_k(\psi_T^{v(i)})$  expresses the Fourier coefficient of the new displacement variable  $\xi = \xi^\psi / R^N$ , whereas in Sec. II the meaning of  $\xi_k(\psi_T^{\text{edge}})$  has been that of the Fourier coefficient of the displacement variable  $\xi^\psi$ .

## V. PERTURBED VACUUM MAGNETIC ENERGY FOR SIMPLY CONNECTED PLASMA CONFIGURATIONS IN THE PRESENCE OF CLOSED AND OPEN FLUX SURFACES

Some changes have to be introduced for the stability calculation of axisymmetric flux-core-spheromak configurations with closed and open flux surfaces, like the one of PROTO-SPHERA<sup>27</sup> (see Fig. 2). The first change is that the plasma-vacuum interface is described by three values of  $\psi_T$ ,

$$\begin{aligned} \psi_T^{v(1)} &= \psi_T^X - \varepsilon_{\text{ST}} \quad (j = N_\psi^{\text{ST}}), \\ \psi_T^{v(2)} &= \psi_T^X + \varepsilon_{\text{SP}} \quad (j = N_\psi^{\text{ST}} + 1) \quad \text{and} \\ \psi_T^{v(3)} &= \psi_T^{\max} - \varepsilon_{\text{symm}} \quad (j = N_\psi^{\text{ST}} + N_\psi^{\text{SP}}). \end{aligned} \quad (36)$$

Over these surfaces, the rotational transforms are, respectively,<sup>20</sup> the logarithmically vanishing  $\ell^{v(1)} = \ell^{v(2)} = \ell_X$  on  $\psi_T^{v(1)}$ ,  $\psi_T^{v(2)}$ , and the nonvanishing  $\ell^{v(3)} = \ell_{\text{symm}}$  on  $\psi_T^{v(3)}$ . The second change is that the perturbed vacuum energy should in principle introduce a coupling among all three surfaces (36): the elements of the magnetic energy matrix  $\tilde{W}$  pertaining to the  $\xi_i^j \xi_k^j$  terms for the mesh points  $i, j = N_\psi^{\text{ST}}, N_\psi^{\text{ST}} + 1$ , and  $N_\psi^{\text{ST}} + N_\psi^{\text{SP}}$  could be nonzero, destroying the block-diagonal structure of the normal-mode equation (3). The vacuum energy treatment is again developed (as in Sec. II) defining, over the cross section of the whole vacuum region surrounding the plasma, the 2D quantities  $\tilde{\Phi}^{nc}$ ,  $\tilde{\Phi}^{ns}$  (10) and introducing, only upon the poloidal contours of the plasma edge cross section, the contour quantities  $\tilde{B}^{nc}$  and  $\tilde{B}^{ns}$  (11). The normal derivative  $\partial/\partial n$  is taken at the ideal conducting shells or at

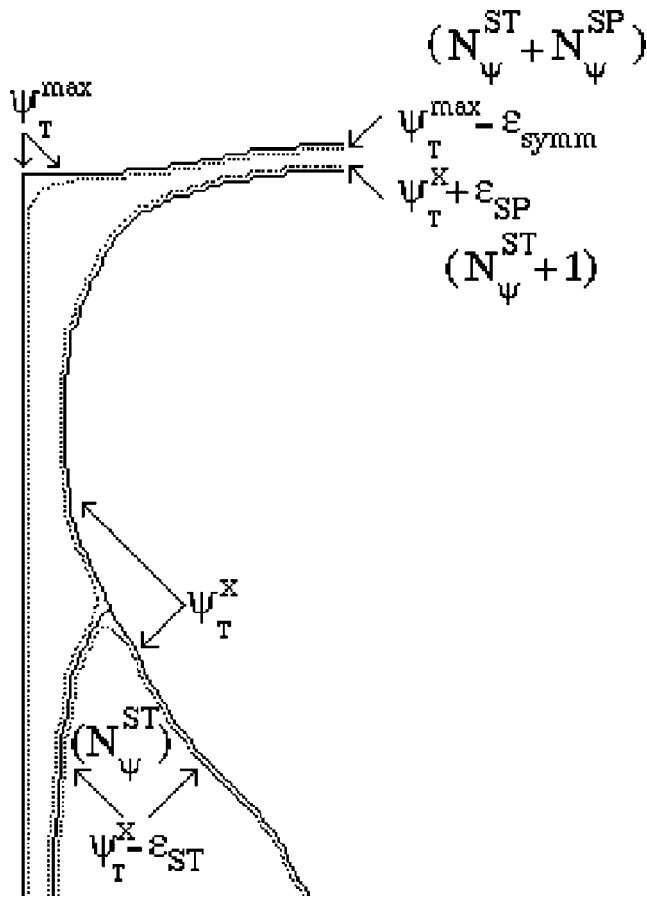


FIG. 2. PROTO-SPHERA equilibrium; full curves represent the magnetic surfaces through the separatrix  $\psi_T^X$  and the axis of symmetry  $\psi_T^{\max}$ , where the Boozer coordinates are singular. Dotted curves represent: the last mesh surface inside the ST ( $j=N_{\psi}^{\text{ST}}$ ); the first mesh surface inside the SP ( $j=N_{\psi}^{\text{ST}}+1$ ); and the last mesh surface near the symmetry axis ( $j=N_{\psi}^{\text{ST}}+N_{\psi}^{\text{SP}}$ ).

the plasma-vacuum interfaces  $S_{\psi}^{v(j)}$ . All surface elements and unitary vectors are oriented out of the vacuum region. Equation (21) is obeyed by the 2D potentials  $\tilde{\Phi}^{nc}$  and  $\tilde{\Phi}^{ns}$ , with boundary conditions (22) on the ideal conducting shells, and

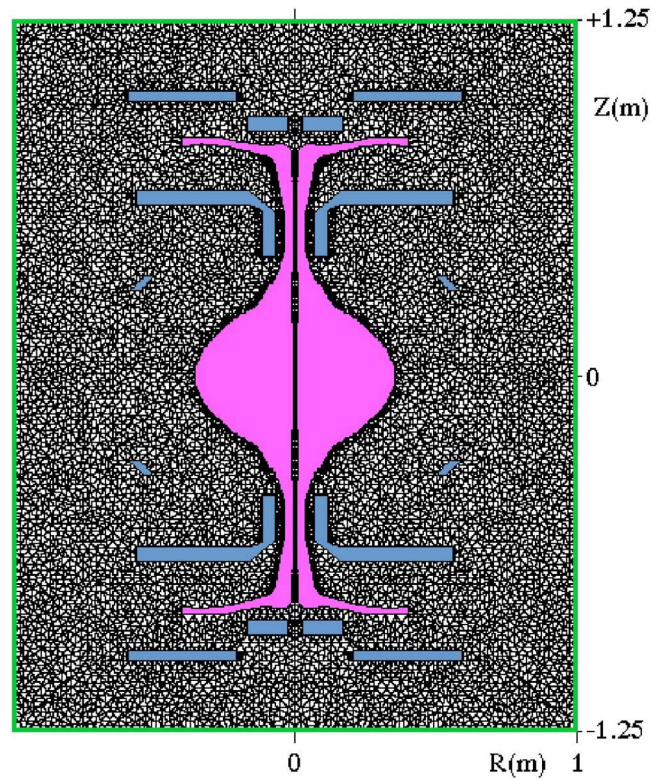


FIG. 3. (Color online) Vacuum 2D finite-element mesh used for PROTO-SPHERA with ideal conducting shells within the vacuum vessel.

(34) and (35) on each of the three  $\psi_T = \psi_T^{v(j)}$  plasma-vacuum interfaces (36). Inside the SP,  $\psi_T^X \leq \psi_T \leq \psi_T^{\max}$ , the function  $\nu(\theta)$  has to be expanded as<sup>17</sup>  $\nu(\psi_T, \theta) = -\sum_{p=0}^{\sim 400} \delta_p^{\psi}(\psi_T) \times \cos(p\pi\{\theta_{\text{EL}}(\psi_T) - \theta\} / [2\pi - 2\theta_{\text{EL}}(\psi_T)] - 1)$ , instead of as the Fourier series of Sec. II. Equation (21) is solved by a 2D finite-element method (Appendix A) in the vacuum region. An example of a 2D finite-element mesh for the evaluation of the vacuum energy in the case of PROTO-SPHERA is shown in Fig. 3. The solutions are expressed, for the three surfaces (36) ( $i, j=1, 2, 3$ ), as

$$\tilde{\Phi}^{nc}(\theta^{(j)})|_{S_{\psi}^{v(j)}} = \sum_{i=1}^3 \sum_k \frac{\xi_k(\psi_T^{v(i)})}{\mu_0} F_k^{c,ji} \left( \theta^{(j)}, \frac{\left[ (\ell^{(i)} m_k - n) R^N \cos[m_k \theta^{(i)} - n\nu(\theta^{(i)})] + \ell^{(i)} N R^{N-1} \left( \frac{\partial R}{\partial \theta} \right) \sin[m_k \theta^{(i)} - n\nu(\theta^{(i)})] \right]}{\sqrt{g(\theta^{(i)})} |\vec{\nabla} \psi_T|_{\theta^{(i)}}} \right); \quad (37)$$

$$\tilde{\Phi}^{ns}(\theta^{(j)})|_{S_{\psi}^{v(j)}} = \sum_{i=1}^3 \sum_k \frac{\xi_k(\psi_T^{v(i)})}{\mu_0} F_k^{s,ji} \left( \theta^{(j)}, \frac{\left[ (\ell^{(i)} m_k - n) R^N \sin[m_k \theta^{(i)} - n\nu(\theta^{(i)})] - \ell^{(i)} N R^{N-1} \left( \frac{\partial R}{\partial \theta} \right) \cos[m_k \theta^{(i)} - n\nu(\theta^{(i)})] \right]}{\sqrt{g(\theta^{(i)})} |\vec{\nabla} \psi_T|_{\theta^{(i)}}} \right), \quad (38)$$

with the poloidal angles  $\theta^{(j)}$  and  $\theta^{(i)}$  labeling, respectively, the “observation” point and the “source” point. Equations (37) and (38) are again the definitions of the reduced Green’s functions; their actual evaluations are given in Eqs. (A8) and (A9) in Appendix A, this time extended over the different plasma-vacuum boundaries. The final result becomes, for ( $i, j=1, 2, 3$ )

$$\delta W_v = \frac{1}{2\mu_0} \sum_{i,j=1}^3 \sum_{l,k} [\xi_l(\psi_T^{v(j)})] \{R_{lk}^{ji}[\xi_k(\psi_T^{v(i)})]\}, \quad (39)$$

with

$$R_{lk}^{ji} = \pi \int_{\theta_{\min}}^{\theta_{\max}} d\theta^{(j)} \times \left[ (\mathcal{L}^{(j)} m_l - n) [R(\theta^{(j)})]^N \cos[m_l \theta^{(j)} - n\nu(\theta^{(j)})] + \mathcal{L}^{(j)} N [R(\theta^{(j)})]^{N-1} \left( \frac{\partial R(\theta^{(j)})}{\partial \theta^{(j)}} \right) \sin[m_l \theta^{(j)} - n\nu(\theta^{(j)})] \right] \\ \times F_k^{c,ji} \left( \theta^{(j)}, \frac{\left[ (\mathcal{L}^{(i)} m_k - n) [R(\theta^{(i)})]^N \cos[m_k \theta^{(i)} - n\nu(\theta^{(i)})] + \mathcal{L}^{(i)} N [R(\theta^{(i)})]^{N-1} \left( \frac{\partial R(\theta^{(i)})}{\partial \theta^{(i)}} \right) \sin[m_k \theta^{(i)} - n\nu(\theta^{(i)})] \right]}{\sqrt{g(\theta^{(i)})} |\vec{\nabla} \psi_T|_{\theta^{(i)}}}} \right) \\ + \pi \int_{\theta_{\min}}^{\theta_{\max}} d\theta^{(j)} \times \left[ (\mathcal{L}^{(j)} m_l - n) [R(\theta^{(j)})]^N \sin[m_l \theta^{(j)} - n\nu(\theta^{(j)})] - \mathcal{L}^{(j)} N [R(\theta^{(j)})]^{N-1} \left( \frac{\partial R(\theta^{(j)})}{\partial \theta^{(j)}} \right) \cos[m_l \theta^{(j)} - n\nu(\theta^{(j)})] \right] \\ \times F_k^{s,ji} \left( \theta^{(j)}, \frac{\left[ (\mathcal{L}^{(i)} m_k - n) [R(\theta^{(i)})]^N \sin[m_k \theta^{(i)} - n\nu(\theta^{(i)})] - \mathcal{L}^{(i)} N [R(\theta^{(i)})]^{N-1} \left( \frac{\partial R(\theta^{(i)})}{\partial \theta^{(i)}} \right) \cos[m_k \theta^{(i)} - n\nu(\theta^{(i)})] \right]}{\sqrt{g(\theta^{(i)})} |\vec{\nabla} \psi_T|_{\theta^{(i)}}}} \right). \quad (40)$$

Equation (40) expresses in matrix form the coupling between the three plasma surfaces (36). However, the vacuum energy contribution from the third magnetic surface  $\psi_T^{v(3)} = \psi_T^{\max} - \varepsilon_{\text{symm}}$ , i.e., the one near the symmetry axis, is effectively decoupled from the first two magnetic surfaces by the closed conducting paths of the plasma-electrode current  $I_e$ , which flows into the electrodes from the feeders on top and bottom of the vacuum vessel (see Fig. 4), with conduction paths assumed axisymmetric. The Laplace equation (21) is solved in the small vacuum regions on top and bottom of the machine—shown shaded in Fig. 4—with the boundary conditions (22) on the ideal conducting shells, and the boundary conditions (34) and (35) rewritten in terms of the “source” Boozer poloidal angle  $\theta^{(3)}$  on the  $\psi_T^{v(3)}$  plasma-vacuum interface.

The solutions  $\tilde{\Phi}^{nc}(\theta^{(3)})|_{S_\psi^{(3)}}$  and  $\tilde{\Phi}^{ns}(\theta^{(3)})|_{S_\psi^{(3)}}$ , restricted upon the  $\psi_T^{v(3)}$  plasma-vacuum interface, are expressed by Eqs. (37) and (38), summing only over the “source” index  $i=3$ , fixing also the “observation” index  $j=3$ , replacing  $\theta^{(j)}$  by  $\theta^{(3)}$  for the poloidal angle and therefore with only  $F_k^{c,33}$  and  $F_k^{s,33}$  acting as reduced Green’s functions. Therefore, the vacuum energy contribution of the magnetic surface  $\psi_T^{v(3)}$  is attributed to the last mesh surface  $j=N_\psi^{\text{ST}}+N_\psi^{\text{SP}}$  as  $\delta W_{v(3)} = \sum_{l,k} [\xi_l(\psi_T^{v(3)})] \{R_{lk}^{v(3)}[\xi_k(\psi_T^{v(3)})]\} / 2\mu_0$ , with  $R_{lk}^{v(3)}$  expressed by Eq. (40), with the same replacements of “source” index  $i=3$  and “observation” index  $j=3$ .

As far as the treatment of the region left by the last mesh surface [see Fig. 5(a)] around the symmetry axis ( $R=0$ ), the asymptotic behavior of the perturbed scalar potential with toroidal mode number  $n$  is  $\lim_{R \rightarrow 0} \tilde{\Phi} \propto R^n$  and  $\lim_{R \rightarrow 0} \partial \tilde{\Phi} / \partial n \propto R^n$ . As a matter of fact, the radial displacement can be derived in general from the perturbed vector potential  $\vec{\nabla}^2 \vec{A} = \mu_0 \vec{j}$ , where  $\vec{j}$  is the perturbed plasma cur-

rent density. Near the symmetry axis, the regular multipolar terms (solutions of the vector Laplace equation) are expressed, in cylindrical coordinates  $(R, \varphi, Z)$ , through the three vectors<sup>28</sup>  $\vec{M}$ ,  $\vec{N}$ , and  $\vec{G}$ . For all of them,  $|\vec{B}| \propto |\vec{\nabla} \wedge \vec{A}| \propto R^{n-1}$ ;

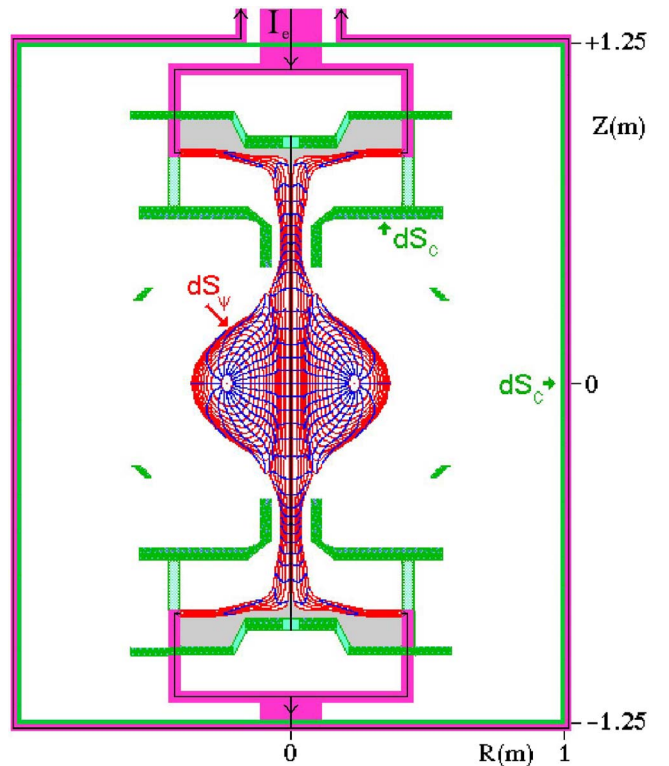


FIG. 4. (Color online) Mesh of Boozer coordinates ( $\psi_T$  radial,  $\theta$  poloidal) for PROTO-SPHERA with conducting shells and conductors of the Screw-Pinch current. The shadings mark the smaller vacuum regions involved in the calculation of the vacuum energy contribution from the last mesh surface  $\psi_T^{v(3)} = \psi_T^{\max} - \varepsilon_{\text{symm}}$ .

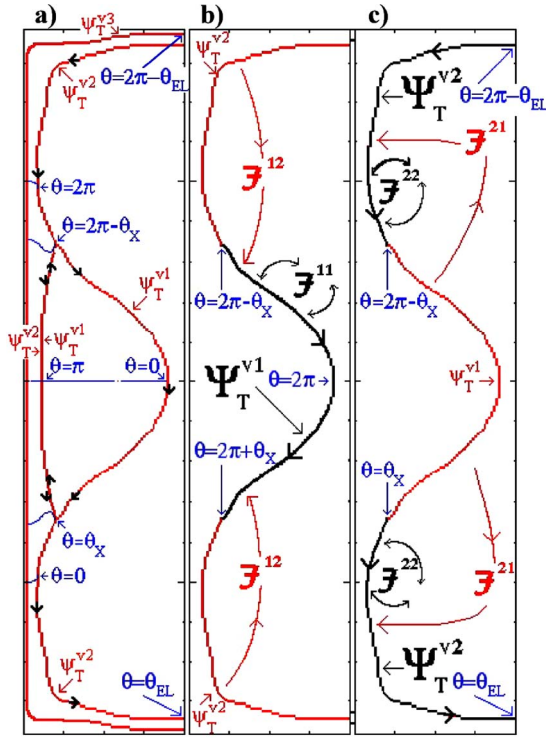


FIG. 5. (Color online) PROTO-SPHERA: (a) flux surfaces (red), values of Boozer poloidal angle (blue), and directions of contour integrations; (b) path for calculation of vacuum energy on  $\psi_T^{v1}$ , in the intermediate range  $[2\pi - \theta_X \leq \theta \leq 2\pi + \theta_X]$  and illustration of the action of reduced Green's functions  $F_k^{11}(\theta^{(1)}, \theta^{(1)})$  and  $F_k^{12}(\theta^{(1)}, \theta^{(2)})$ ; (c) path for calculation of vacuum energy on  $\psi_T^{v2}$ , in the two disconnected ranges of poloidal Boozer angles  $[2\pi - \theta_{EL} \geq \theta > 2\pi - \theta_X]$  and  $[\theta_X > \theta \geq \theta_{EL}]$ , and illustration of the action of reduced Green's functions  $F_k^{21}(\theta^{(2)}, \theta^{(1)})$  and  $F_k^{22}(\theta^{(2)}, \theta^{(2)})$ .

therefore, the asymptotic behavior of the radial displacement variable is  $\lim_{R \rightarrow 0} \xi^\psi \propto R^n$ , for both FCS as well as for CKF configurations. In the numerical code:<sup>20</sup>

- Either the last mesh surface, located at  $\psi_T = \psi_T^{\max} - \varepsilon_{\text{symm}}$ , is far enough from the symmetry axis and the simply connected conducting shell is closed there by an infinitesimally thin wire, which enforces the condition  $\partial\tilde{\Phi}/\partial n = 0$  at  $R=0$ ; in this case, the integrals for evaluating the matrix coefficients  $R_{lk}$  of Eq. (40) are extended over all the poloidal angles  $\theta_{EL} \leq \theta^{(j)} \leq 2\pi - \theta_{EL}$ .
- Or the last mesh surface, located at  $\psi_T = \psi_T^{\max} - \varepsilon_{\text{symm}}$ , is very near the symmetry axis and a vacuum region, already satisfying  $\partial\tilde{\Phi}/\partial n = 0$  at  $R=0$ , can replace the plasma in this very small region; in this latter case, the integrals for evaluating  $R_{lk}$  are extended only over the poloidal angles  $\theta^{(j)}$ , where the last mesh surface exceeds a given distance from  $R=0$ . The effect upon the stability threshold of the two different assumptions is only marginal, as will be discussed in a forthcoming paper.

As a consequence, the only remaining coupling in the vacuum energy could be the one between the last mesh surface inside the ST at  $\psi_T^{v(1)} = \psi_T^X - \varepsilon_{ST}$  and the first mesh surface inside the SP at  $\psi_T^{v(2)} = \psi_T^X + \varepsilon_{SP}$ —see Fig. 2. However, these two surfaces have been chosen to be as near as numerically possible to the ST-SP interface, and such that they have

the same logarithmically vanishing rotational transform,<sup>17</sup>  $\ell^{v(1)} = \ell^{v(2)} = \ell_X$ : it is therefore possible to overlap them, which means for the reduced Green's functions

$$\lim_{\varepsilon_{ST}, \varepsilon_{SP} \rightarrow 0} F_k^{s,12}(\theta^{(1)}, \theta) + F_k^{s,11}(\theta^{(1)}, \theta) = 0 \quad (41)$$

and

$$\lim_{\varepsilon_{ST}, \varepsilon_{SP} \rightarrow 0} F_k^{s,21}(\theta^{(2)}, \theta) + F_k^{s,22}(\theta^{(2)}, \theta) = 0 \quad (42)$$

(with  $\theta^{(1)}$  and  $\theta^{(2)}$  representing the “observation” point) for all the range  $(\theta_X, 2\pi - \theta_X)$  that the poloidal Boozer “source” angles  $\theta$  take along the common magnetic separatrix, see Fig. 5. Furthermore, the continuity condition on the radial plasma displacement variable imposes<sup>20</sup>

$$\xi_i(\psi_T^{v(1)}) = \xi_i(\psi_T^{v(2)}). \quad (43)$$

Equations (41)–(43) imply that neither the coupling between  $\psi_T^{v(1)}$  nor  $\psi_T^{v(2)}$  destroys the block-diagonal structure of the normal-mode equation (3). The Laplace equation (21) is solved in the large vacuum region shown in Fig. 5. The boundary conditions (22) apply on the ideal conducting shells, whereas the boundary conditions are expressed by Eqs. (34) and (35), replacing  $\ell^{v(i)}$  by  $\ell_X$  and the “source” angle  $\theta^{(i)}$  by  $\theta^u$  on a unique (merged) plasma-vacuum interface  $t$ , respectively, composed of the SP surface ( $\psi_T^u = \psi_T^{v(2)}$ ) in the two disconnected ranges of poloidal Boozer angles  $[2\pi - \theta_X < \theta^u = \theta^{v(2)} \leq 2\pi - \theta_{EL}]$  and  $[\theta_{EL} \leq \theta^u = \theta^{v(2)} < \theta_X]$  and by the ST surface ( $\psi_T^u = \psi_T^{v(1)}$ ), in the intermediate range  $[2\pi - \theta_X \leq \theta^u = \theta^{v(1)} \leq 2\pi - \theta_X]$ .

The solutions, restricted upon the merged  $\psi_T^u$  plasma-vacuum interface, are expressed, upon  $\psi_T^u = \psi_T^{v(1)}$ , as a function of the poloidal angle  $\theta^{(1)}$  by Eqs. (37) and (38), fixing the “observation” index  $j=1$ , summing only over  $i=u$  (i.e., replacing the “source” angle  $\theta^{(i)}$  with  $i=1,2$  by  $\theta^u$ ), replacing  $\ell^{v(i)}$  by  $\ell_X$  and therefore using only  $F_k^{c,1u}$  and  $F_k^{s,1u}$  as the reduced Green's functions. Upon  $\psi_T^u = \psi_T^{v(2)}$ , the solutions are functions of the poloidal angle  $\theta^{(2)}$  by Eqs. (37) and (38), with the “observation” index set to  $j=2$ , summing only over  $i=u$  (i.e., replacing the “source” angle  $\theta^{(i)}$  by  $\theta^u$ ) and therefore using only  $F_k^{c,2u}$  and  $F_k^{s,2u}$  as reduced Green's functions. The reduced Green's functions for the merged  $\psi_T^u$  plasma-vacuum interface are defined as

$$F_k^{s,j1} = F_k^{s,j1}$$

when the “source” angle is  $\theta^u = \theta^{v(1)}$ ;

$$F_k^{s,j2} = F_k^{s,j2}$$

when the “source” angle is  $\theta^u = \theta^{v(2)}$ . The two vacuum energy contributions are, respectively,

- $\delta W_{v(1)} = \sum_{l,k} [\xi_l(\psi_T^{v(1)})] [R_{lk}^{1u}] [\xi_k(\psi_T^{v(1)})] / 2\mu_0$ , with  $R_{lk}^{1u}$  expressed by Eq. (40), with the same choices of the “source” index  $i=u$  (i.e., replacing the “source” angle  $\theta^{(i)}$  with  $i=1,2$  by  $\theta^u$ ), the “observation” index  $j=1$ ,  $\ell^{v(i)} = \ell_X$  and with  $\theta_{\min} = 2\pi - \theta_X$ ,  $\theta_{\max} = 2\pi + \theta_X$ ;

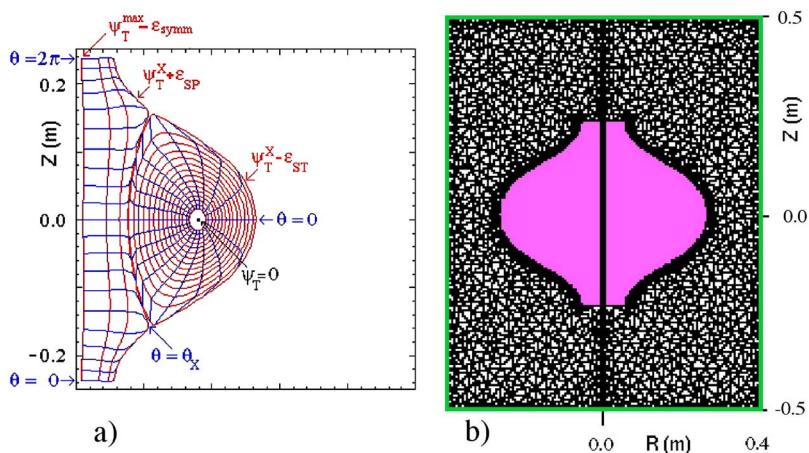


FIG. 6. (Color online) TS-3 flux-core-spheromak configuration, composed of ST and SP, with  $I_{\text{ST}}=50$  kA and  $I_e=40$  kA: (a) Boozer coordinates cross section, showing the angles  $\theta_X$  labeling the lower regular X-point and  $\theta=0$  and  $\theta=2\pi$  that mark the position of the two plasma-electrode interfaces; (b) vacuum 2D finite element mesh (shaded), with conducting shells marked in green.

- $\delta W_{v(2)} = \sum_{l,k} [\xi_l(\psi_T^{v(2)})] \{R_{lk}^{2l}\} [\xi_k(\psi_T^{v(2)})] / 2\mu_0$  with  $R_{lk}^{2l}$  expressed by Eq. (40), with the same choices of the “source” index  $i=u$  (i.e., replacing the “source” angle  $\theta^{(i)}$  with  $i=1,2$  by  $\theta^u$ ), the “observation” index  $j=2$ ,  $l^{(i)}=l_X$  and by summing over the two disjoint integration ranges  $[\theta_{\min}=2\pi-\theta_{\text{EL}}, \theta_{\max}=2\pi-\theta_X]$  and  $[\theta_{\min}=\theta_X, \theta_{\max}=\theta_{\text{EL}}]$ .

## VI. RESULTS FOR FLUX-CORE SPHEROMAKS

The new version of the STABLE code<sup>20</sup> which works for the simply connected flux-core spheromak, illustrated in Sec. IV and V, has been dubbed “STABLECN.” A preliminary summary of the results of the ideal MHD stability code STABLECN applied to flux-core spheromaks with a singular X-point on the symmetry axis (and therefore with a plasma-vacuum interface composed of three values of  $\psi_T$ ) has already been presented in Ref. 27, which describes in broad terms the PROTO-SPHERA project. A comparison between the codes STABLE and STABLECN is presented here for a case of the Tokyo University Spherical Torus No. 3 (TS-3) flux-core-spheromak experiment,<sup>29</sup> which was not endowed with a singular X-point on the symmetry axis: TS-3 did not have plasma disks inside separate electrode chambers, but its central plasma column was a screw pinch fed by cylindrical electrodes [see Fig. 6(a)]. Therefore, the plasma-vacuum interface of TS-3 is described by just two values of  $\psi_T$ :  $\psi_T^{v(1)} = \psi_T^X - \epsilon_{\text{ST}}$  for  $i=N_{\psi}^{\text{ST}}$  and  $\psi_T^{v(2)} = \psi_T^X + \epsilon_{\text{SP}}$  for  $i=N_{\psi}^{\text{ST}}+1$ , which

have again been chosen so that they have the same logarithmically vanishing rotational transform<sup>17</sup>  $l^{v(1)}=l^{v(2)}=l_X$ . On the other hand, the symmetry axis  $\psi_T^{v(3)} = \psi_T^{\max} - \epsilon_{\text{symm}}$  ends on the feeding electrodes. Therefore, it is possible to investigate the stability of the TS-3 flux-core-spheromak experiment also with the STABLE code (already validated against the analytic Solovév equilibria) and then to validate the stability results obtained with STABLECN. The first equilibrium<sup>29</sup> of TS-3 considered for the ideal MHD stability calculation has a longitudinal pinch current  $I_e=40$  kA, a toroidal ST current  $I_{\text{ST}}=50$  kA, and a volume averaged beta inside the ST  $\beta_{\text{ST}}=12.0\%$  (defined as  $\beta_{\text{ST}}=2\mu_0\langle p \rangle_{\text{ST}} / \langle B^2 \rangle_{\text{ST}}$ ). The conducting shell is limited to the vacuum vessel, as shown in Fig. 6(b). In this section, the results for the growth rate are expressed as the ratio between the square of the growth rate of the instability  $\omega^2$  and the Alfvén rate,  $\omega_A^2 = B_0^2 / \mu_0 \rho_0 R_0^2$ , where  $B_0$  is the magnetic field on the ST magnetic axis  $R_0$  and  $\rho_0$  is the plasma mass density (assumed constant). The positive  $\omega^2$  provided by STABLE  $\omega^2 / \omega_A^2 = +1.33 \times 10^{-7}$ , when the regularity condition  $\xi^{\psi}(\psi_T^{\max})=0$  is imposed, becomes an unstable (negative)  $\omega^2 / \omega_A^2 = -1.03$  when no condition on  $\xi^{\psi}(\psi_T^{\max})$  is applied. STABLECN, which does not need any constraint on  $\xi(\psi_T^{\max})$ , provides a stable plasma with  $\omega^2 = +1.35 \times 10^{-7}$ , which is quite similar in eigenvalue to the one obtained by STABLE, when  $\xi^{\psi}(\psi_T^{\max})=0$  is imposed.

Figure 7 shows the perturbed displacement plots upon a

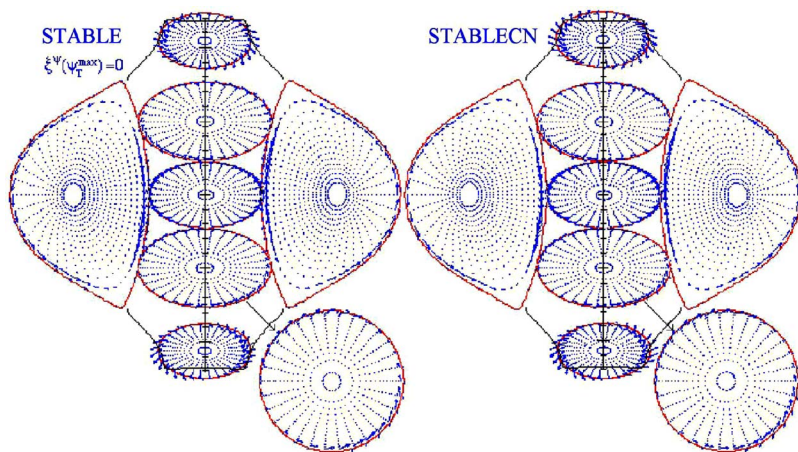


FIG. 7. (Color online) Displacement arrow plots for the largest eigenvalue mode with  $n=1$  for TS-3 with  $I_e=40$  kA,  $I_{\text{ST}}=50$  kA, and  $\beta \approx 12\%$ . The left-hand side plots are calculated by STABLE, with the condition  $\xi^{\psi}(\psi_T^{\max})=0$ ; the right-hand side plots are calculated by STABLECN.

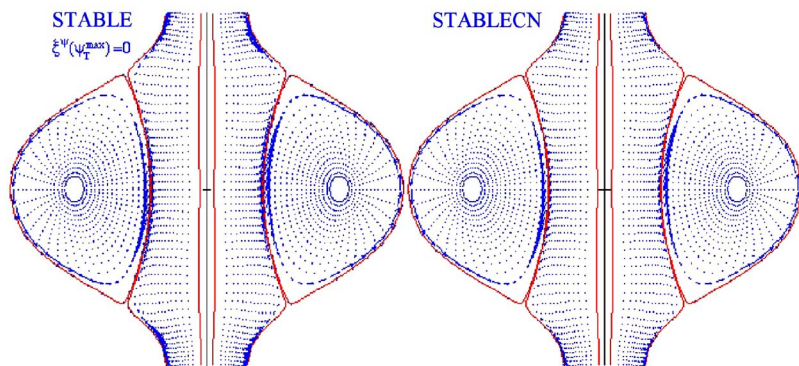


FIG. 8. (Color online) Displacement arrow plots for the largest eigenvalue mode with  $n=1$  for TS-3 with  $I_e = 40$  kA,  $I_{ST}=50$  kA, and  $\beta \approx 12\%$ , all upon a poloidal cross section. The left-hand side plots are calculated by STABLE, with the condition  $\xi^\psi(\psi_T^{\max})=0$ ; the right-hand side plots are calculated by STABLECN.

poloidal plane cross section inside the ST and upon some horizontal plane cross sections inside the SP. It confirms that the code STABLE, with the condition  $\xi^\psi(\psi_T^{\max})=0$  at the symmetry axis, and the code STABLECN calculate roughly the same eigenfunction, namely an oscillating motion around the  $q=1$  resonance, which is present inside the ST as well as inside the SP. Figure 8 shows that, in the case of TS-3, the similarity of the two eigenfunctions is also clear when the displacement plots are shown upon the poloidal cross section, inside both the ST and the SP.

In the case of TS-3, with  $I_e=40$  kA,  $I_{ST}=100$  kA and  $\beta=13.8\%$ , STABLE calculates—even forcing the regularity condition  $\xi^\psi(\psi_T^{\max})=0$ —an unstable plasma. The negative  $\omega^2$  provided by STABLE  $\omega^2/\omega_A^2=-1.1$ , when  $\xi^\psi(\omega_T^{\max})=0$  is imposed, becomes  $\omega^2/\omega_A^2=-3.92$  when no condition on  $\xi^\psi(\psi_T^{\max})$  at the symmetry axis is applied. STABLECN provides an unstable plasma with  $\omega^2=-2.73$ . Figure 9 shows the perturbed upon a poloidal plane cross sections inside the ST and upon some horizontal plane cross sections inside the screw pinch. Figure 10 shows that the similarity of the two eigenfunctions obtained by the STABLE code with the regularity condition  $\xi^\psi(\psi_T^{\max})=0$  and by the code STABLECN is also clear when the displacement plots are shown upon the poloidal cross section, inside both the ST and the SP. The ideal MHD stability calculations broadly agree with the experimental results,<sup>29</sup> confirming the experimental observation that the TS-3 flux-core spheromak did not achieve a toroidal ST current much higher than  $I_{ST}=50$  kA and that its ST was

limited to an aspect ratio not lower than  $A=1.6$ . For all the equilibria of TS-3, the code STABLE with the regularity condition  $\xi^\psi(\psi_T^{\max})=0$  at the symmetry axis and the code STABLECN calculate very similar results for the ideal MHD stability.

## VII. CONCLUSIONS

It is well known that in an axisymmetric magnetoplasma equilibrium, when conducting shells are placed at a distance from the plasma-vacuum interface  $\psi_T^{\text{edge}}$ , which is therefore free to move,  $\xi^\psi(\psi_T^{\text{edge}}) \neq 0$ , the ideal MHD normal-mode equation is modified by the free-boundary vacuum magnetic energy through an additional term at the plasma-vacuum interface,  $\delta W_v = \sum_{l,k} \{ \xi_l(\psi_T^{\text{edge}}) \} \{ R_{lk} \} \{ \xi_k(\psi_T^{\text{edge}}) \} / 2\mu_0$ ; for doubly connected plasma topologies, such a term does not destroy the block-diagonal structure of the normal-mode equation. For every (separable) toroidal number  $n$ , the 2D magnetic scalar potential perturbation  $\tilde{\Phi}^{n(c,s)}$  satisfies the Laplace equation in the vacuum region, taking into account the boundary conditions on the conducting shells. This leads naturally to the use of the Green's function method for the evaluation of the coupling coefficients  $R_{lk}$ , where the calculation is reduced to an integration [see Eq. (26)] along the plasma-vacuum interface. In particular, solving the Laplace equation for  $\tilde{\Phi}^{n(c,s)}$  defines the reduced Green's functions  $F_k^{(c,s)}$ , as the links (23) and (24) between  $\tilde{\Phi}^{n(c,s)}(\theta^{\text{edge}})$  and the poloidal Fourier components  $\xi_k(\psi_T^{\text{edge}})$ .

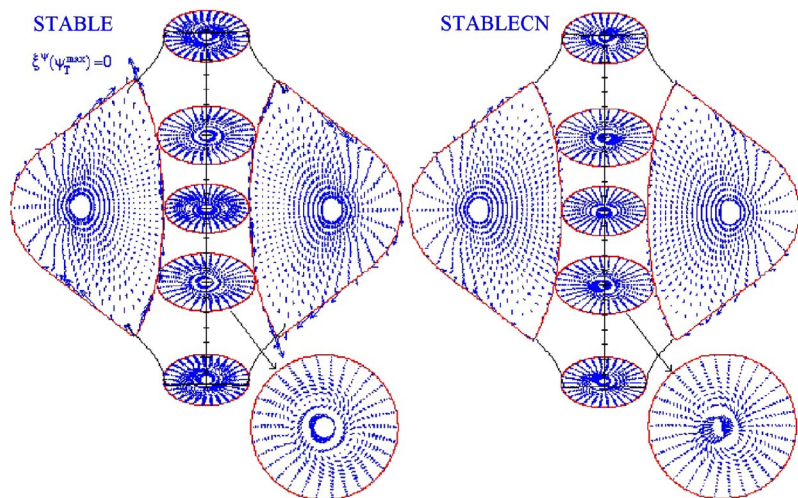


FIG. 9. (Color online) Displacement arrow plots for the largest eigenvalue mode with  $n=1$  for TS-3 with  $I_e = 40$  kA,  $I_{ST}=100$  kA, and  $\beta \approx 14\%$ . The left-hand side plots are calculated by STABLE, with the condition  $\xi^\psi(\psi_T^{\max})=0$ ; the right-hand side plots are calculated by STABLECN.

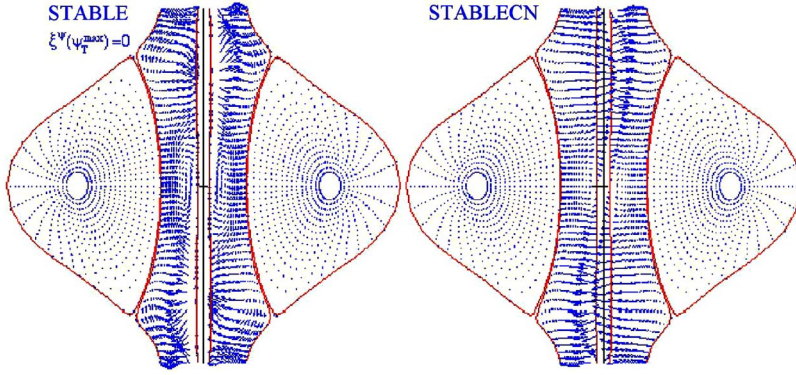


FIG. 10. (Color online) Displacement arrow plots for the largest eigenvalue mode with  $n=1$  for TS-3 with  $I_e=40$  kA,  $I_{ST}=100$  kA, and  $\beta \approx 14\%$ , all upon a poloidal cross section. The left-hand side plots are calculated by STABLE, with the condition  $\xi^\psi(\psi_T^{\max})=0$ ; the right-hand side plots are calculated by STABLECN.

The use of the 2D finite-element method for solving the Laplace equation for  $\tilde{\Phi}^{n\{c,s\}}$  in the vacuum region allows for the simple evaluation (A8) and (A9) of the reduced Green's function,  $F_k^{c,s}$ ; it furthermore simplifies the analytical treatment and therefore allows for simpler expressions in cases in which a more complicated topology has to be considered. Examples of such equilibria are flux-core spheromaks (FCS) and spherical tori with a plasma central column (ST-PCC), where a magnetic separatrix divides a spherical torus, with closed field lines, from a central screw pinch discharge, with open field lines that end on the sustaining electrodes. These configurations pose two problems: (i) the plasma-vacuum interface is composed by multiple flux surfaces  $\psi_T^{v(i)}$  (up to three for the cases considered here) and (ii) the plasma extends up to the symmetry axis. The problem (i) of multiple plasma-vacuum interfaces introduces a coupling between the different surfaces  $\psi_T^{v(j)}$  in the perturbed vacuum magnetic energy additional term,  $\delta W_v = \sum_{i,j=1}^3 \sum_{l,k} [\xi(\psi_T^{v(j)})] \{R_{lk}^{ji}\} \times [\xi_k(\psi_T^{v(i)})] / 2\mu_0$ , which not only complicates the evaluation (40) of the coupling coefficients  $R_{lk}^{ji}$  from the reduced Green's function  $F_k^{c,s,ji}$ , but (in principle) destroys the block-diagonal structure of the normal-mode equation. However, it has been shown that the term  $\delta W_{v(3)}$  pertaining to the plasma-vacuum interface  $\psi_T^{v(3)}$ —branching to annular electrodes from the symmetry axis—is completely decoupled from the other plasma-vacuum interfaces  $\psi_T^{v(1)}$  and  $\psi_T^{v(2)}$ . As for the latter, their proximity along the ST-SP interface, the continuity of the angles  $\theta$  and  $\phi$  across them,<sup>17</sup> the choice of selecting them with the same logarithmically small rotational transform,<sup>17</sup>  $\iota^{v(1)} = \iota^{v(2)} = \iota_X$ , and the continuity<sup>20</sup> of the normal variable  $\xi^\psi$  allows for simplifications between the reduced Green's function  $F_k^{c,s,ji}$  (with  $i, j=1, 2$ ) and therefore permits effectively “uncoupled” evaluations for  $\delta W_{v(1)}$  and  $\delta W_{v(2)}$ ; the coupling coefficients  $R_{lk}^{1i}$  and  $R_{lk}^{2i}$  (with  $i=1, 2$ ) are calculated using a unique (merged) plasma-vacuum interface composed by the ST surface  $\psi_T^{v(1)}$  in the range of poloidal Boozer angles between the upper and lower regular X-points, and by the SP surface  $\psi_T^{v(2)}$ , in the two disconnected ranges of poloidal angles between each electrode and its nearest regular X-point.

The problem (ii) of the plasma extending up to the symmetry axis—that can even host a singular X-point at the plasma-vacuum interface—is solved through a change in the radial and binormal displacement variables,  $\xi^\psi = \xi R^N$ , with

$N=2$  and  $\eta^\psi = \eta B$ , respectively; with these choices there is no need to force any regularity condition either on the symmetry axis or on the singular X-points.

As an illustration of the method, an evaluation of the ideal MHD stability is provided for the experimental results of the TS-3 flux-core-spheromak experiment: the calculations confirm the observations that TS-3 did achieve a current not much higher than  $I_{ST}=50$  kA and that its ST was limited to an aspect ratio not lower than  $A=1.6$ .

#### APPENDIX A: FINITE-ELEMENT METHOD USED TO CALCULATE THE REDUCED GREEN'S FUNCTIONS $F_k^c$ AND $F_k^s$

As was illustrated in Sec. II, the perturbed vacuum magnetic energy is obtained by solving, for any (separable) toroidal number  $n$ , the Laplace equation (21) for the perturbed scalar potential  $\tilde{\Phi}$  in the 2D cross section  $\Omega$  of the whole vacuum domain, with Neumann boundary conditions (16) and (17) on the plasma-vacuum interface  $S_\psi$ :  $\partial\tilde{\Phi}/\partial n|_{S_\psi} = g$ , where  $g$  is one of the functions,

$$g = \frac{\cos[m_k\theta' - n\nu(\theta')]}{\sqrt{g(\theta')}|\nabla\psi_T|_{\theta'}} \quad \text{or} \quad g = \frac{\sin[m_k\theta' - n\nu(\theta')]}{\sqrt{g(\theta')}|\nabla\psi_T|_{\theta'}}. \quad (\text{A1})$$

Using the variational formulation, a straightforward calculation shows that the problem of finding  $\tilde{\Phi}$  such that

$$\frac{1}{R} \frac{\partial}{\partial R} \left( R \frac{\partial \tilde{\Phi}}{\partial R} \right) + \frac{\partial^2 \tilde{\Phi}}{\partial Z^2} - \frac{n^2}{R^2} \tilde{\Phi} = 0 \quad \text{with} \quad \frac{\partial \tilde{\Phi}}{\partial n} \Big|_{S_\psi} = g \quad (\text{A2})$$

is equivalent to the problem of finding

$$\int_{\Omega} \frac{\partial \tilde{\Phi}}{\partial R} \frac{\partial \Theta}{\partial R} + \frac{\partial \tilde{\Phi}}{\partial Z} \frac{\partial (\tilde{\Phi} \Theta)}{\partial Z} + \frac{n^2 (\tilde{\Phi} \Theta)}{R^2} R dR dZ = \int_S \frac{\partial \tilde{\Phi}}{\partial n} \Theta dS, \quad \forall \Theta. \quad (\text{A3})$$

The finite-element method consists in solving an approximated problem onto the vertices of a conforming mesh of the computational domain. The complexity of the geometry of the boundary of the vacuum domain requires finite-

element quite isotropic-like triangle elements and the excluded structured mesh using, for example, quadrangle elements. To do that, a very efficient mesh generator, the so-called “triangle,”<sup>30</sup> a freeware developed by Carnegie Mellon University, has been used. “Triangle” is able to create a good quality triangular mesh. Now one supposes that the nonoverlapping triangular mesh recovers the vacuum domain,  $\cup_{i=1,N}T_i$ . On the set of the vertices  $a_j, j=1, M$  of the triangles of the mesh, set functions are defined, such that  $\chi_j(a_k)=\delta_{jk}$ , with  $\chi_j$  continuous and linear piecewise on each triangle  $T_i$ . The approximated problem consists in searching the solution in the space spanned by the basis functions,

$$\tilde{\Phi}(x) = \sum_{j=1,M} \tilde{\Phi}_j \chi_j(x), \quad (\text{A4})$$

where  $\tilde{\Phi}_j, j=1, M$  are the components of the approximate solution on the basis functions. Replacing (A4) in the variational form (A3), the following linear system is written:

$$\begin{aligned} \sum_{j=1,M} \tilde{\Phi}_j(g) \int_{\Omega} \frac{\partial \chi_j}{\partial R} \frac{\partial \chi_i}{\partial R} + \frac{\partial \chi_j}{\partial Z} \frac{\partial \chi_i}{\partial Z} + n^2 \frac{\chi_j \chi_i}{R^2} R dR dZ \\ = \int_S g \chi_i dS, \quad \forall i \leq M \end{aligned} \quad (\text{A5})$$

and the total vacuum energy is then obtained by the expression

$$\begin{aligned} \delta W_v(g) = \sum_{i,j=1,M} \tilde{\Phi}_j(g) \tilde{\Phi}_i(g) \int_{\Omega} \frac{\partial \chi_j}{\partial R} \frac{\partial \chi_i}{\partial R} + \frac{\partial \chi_j}{\partial Z} \frac{\partial \chi_i}{\partial Z} \\ + n^2 \frac{\chi_j \chi_i}{R^2} R dR dZ = \sum_i \tilde{\Phi}_i(g) \int_S g \chi_i dS. \end{aligned} \quad (\text{A6})$$

The coefficients of the matrix

$$A_{ij} = \int_{\Omega} \frac{\partial \chi_j}{\partial R} \frac{\partial \chi_i}{\partial R} + \frac{\partial \chi_j}{\partial Z} \frac{\partial \chi_i}{\partial Z} + n^2 \frac{\chi_j \chi_i}{R^2} R dR dZ \quad (\text{A7})$$

are equal to zero, if the vertices  $i$  or  $j$  have no triangle in common. The other coefficients are computed numerically using the Gauss formula in each triangle. For the right-hand side of (A5), it is necessary to compute  $\oint_{l_j} \chi_j \cos[m_l \theta - n\nu(\theta)]$  and  $\oint_{l_j} \chi_j \sin[m_l \theta - n\nu(\theta)]$ , corresponding to the contribution of the various poloidal mode numbers  $m_l$ . A quadrature formula is then used on the whole support of the basis functions:  $\chi_j, j=1, M$ . For example,  $\oint_{l_j} \chi_j \cos[m_l \theta - n\nu(\theta)] \cos[m_l \theta_j - n\nu(\theta_j)] \Delta \theta_j$ , where  $\theta_j$  is the location of the vertices of the triangle defining the plasma-vacuum interface and  $\Delta \theta_j$  is the length of the corresponding edges. In order to exploit the sparse structure (A7) of the matrix  $\vec{\mathbf{A}}$ , a renumbering algorithm of the nodes has been used. The bandwidth of matrix  $\vec{\mathbf{A}}$  is then drastically reduced and yields minimal memory requirements. After a Cholesky decomposition, each linear system (A5), corresponding to each right-hand side (A1), is solved by forward and backward substitution. The operators become

$$F_k^c \left( \theta, \frac{\cos[m_k \theta' - n\nu(\theta')]}{\sqrt{g(\theta')} |\vec{\nabla} \psi_T|_{\theta'}} \right) = \sum_{j=1,M} \tilde{\Phi}_j \left( \frac{\cos[m_k \theta' - n\nu(\theta')]}{\sqrt{g(\theta')} |\vec{\nabla} \psi_T|_{\theta'}} \right) \times \chi_j(R(\theta), Z(\theta)), \quad (\text{A8})$$

$$F_k^s \left( \theta, \frac{\sin[m_k \theta' - n\nu(\theta')]}{\sqrt{g(\theta')} |\vec{\nabla} \psi_T|_{\theta'}} \right) = \sum_{j=1,M} \tilde{\Phi}_j \left( \frac{\sin[m_k \theta' - n\nu(\theta')]}{\sqrt{g(\theta')} |\vec{\nabla} \psi_T|_{\theta'}} \right) \times \chi_j(R(\theta), Z(\theta)), \quad (\text{A9})$$

where  $R(\theta), Z(\theta)$  describe the plasma-vacuum interface when  $\theta \in (0, 2\pi)$ . The vacuum magnetic energy becomes (25), with  $R_{lk}$  defined by (26). At this point, the computation of coefficients  $R_{lk}$  is reduced to the integration of  $\oint_{l_j} \chi_j \cos[m_l \theta - n\nu(\theta)]$  and  $\oint_{l_j} \chi_j \sin[m_l \theta - n\nu(\theta)]$ , which is performed with the previous procedure.

## APPENDIX B: COMPARISON WITH THE STABILITY RESULTS OF THE ANALYTICAL SOLOVEV EQUILIBRIA

The axisymmetric analytical Solovév MHD equilibrium solutions<sup>22</sup> have long been chosen as a benchmark<sup>21</sup> for all ideal MHD stability codes. The reason is that they permit a configurational variety of “approximate inverse aspect ratio”  $\varepsilon$ , cross-section elongation  $\kappa$ , and safety factor at the magnetic axis  $q_0=1/l_0$  (inverse of the rotational transform), while being independent of the numerical accuracy of the equilibrium convergence. Geometric and magnetic scaling parameters of the Solovév solutions are the position of the magnetic axis  $R_0$  and the toroidal field strength  $B_0$  on the magnetic axis, both normalized to 1. They obey the Grad-Shafranov equation for the poloidal flux  $\psi = \int \vec{B} \cdot d\vec{S}_p$  in cylindrical coordinates  $(R, \varphi, Z)$ ,

$$\frac{\partial^2 \psi}{\partial R^2} + \frac{\partial^2 \psi}{\partial Z^2} - \frac{1}{R} \frac{\partial \psi}{\partial R} = -4\pi^2 \mu_0 R^2 \frac{\partial p(\psi)}{\partial \psi} - 4\pi^2 f(\psi) \frac{\partial f(\psi)}{\partial \psi}, \quad (\text{B1})$$

with the kinetic pressure

$$p(\psi) = \frac{(1 + \kappa^2) B_0}{2\pi \mu_0 \kappa R_0^2 q_0} \psi$$

and the normalized poloidal current  $f(\psi)=B_0 R_0 = \text{const}$  as source terms. The second source term means that the plasma poloidal beta is 1:  $\beta_p=1$ . The flux surfaces of the Solovév equilibria are

$$\psi = \frac{\pi B_0}{q_0} \left\{ \varepsilon^2 \kappa R_0^2 - \frac{1}{k R_0^2} \left[ R^2 Z^2 + \frac{\kappa^2}{4} (R^2 - R_0^2)^2 \right] \right\}, \quad (\text{B2})$$

so that  $\psi=0$  corresponds to the plasma edge and

$$\psi_{\text{axis}} = \pi B_0 \varepsilon^2 \kappa R_0^2 / q_0. \quad (\text{B3})$$

The true inverse aspect ratio of any configuration is

$$\frac{a}{R} = \frac{2}{(\sqrt{1+2\varepsilon} + \sqrt{1-2\varepsilon})^2}, \quad (\text{B4})$$

which coincides with  $\varepsilon$  only in the limit  $\varepsilon \rightarrow 0$ , whereas it is unity for  $\varepsilon=1/2$ .

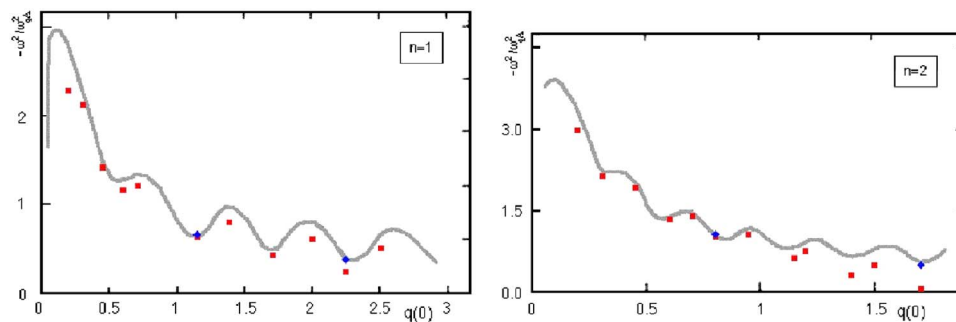


FIG. 11. (Color online) Comparison of  $-\omega^2/\omega_{qA}^2$  for free-boundary stability results (without any ideal conducting shell near the plasma) between the compressible stability code STABLE (squares) and the ERATO code (Ref. 21) (line), for the Solovév equilibrium with  $\varepsilon=1/3$  and  $\kappa=2$ . The toroidal mode numbers are  $n=1$  and 2, respectively. All the results from STABLE are obtained with a spectrum of poloidal mode numbers in the range  $m_l=[-3, +7]$  and a few cases with  $m_l=[-5, +15]$  (diamonds).

A remarkable property of the Solovév analytical MHD equilibria is that the ratio between the safety factor at the plasma edge  $q_{\text{edge}}$  and the safety factor at the magnetic axis  $q_0$  depends only upon the “approximate inverse aspect ratio”  $\varepsilon$ . The “conformal shape” of a closed ideal conducting axisymmetric shell, surrounding at a finite distance the Solovév equilibrium, is determined by the same equation (B2), provided negative values of  $\psi_W$  are introduced ( $\psi=0$  being the plasma edge), such that the normalized plasma-shell distance becomes

$$\Lambda = \sqrt{-\psi_W/\psi_{\text{axis}}}. \quad (\text{B5})$$

The absence of any ideal conducting shell around the plasma is described by  $\Lambda \rightarrow \infty$ .

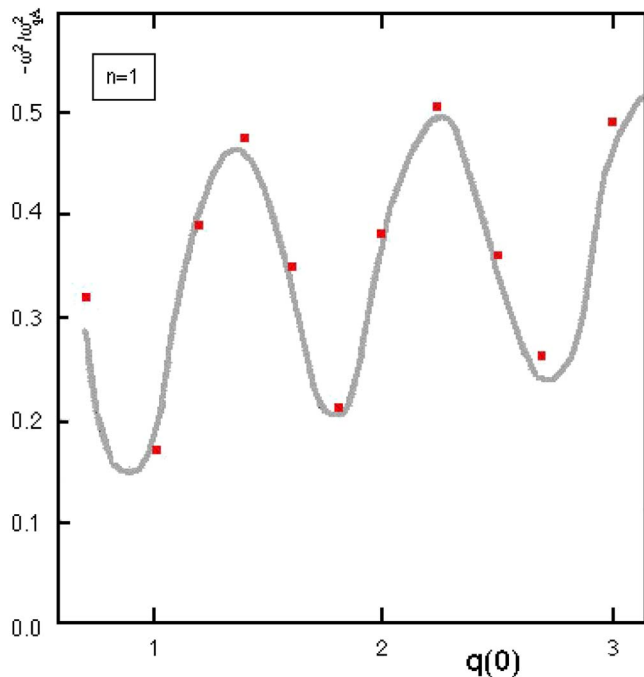


FIG. 12. (Color online) Comparison of  $-\omega^2/\omega_{qA}^2$  for free-boundary stability results (with an ideal conducting shell at  $\Lambda=2$ ) between the compressible stability code STABLE (dots) and the Kerner and PEST codes (Ref. 21) (line), for the Solovév equilibrium with  $\varepsilon=1/6$  and  $\kappa=1$ . The toroidal mode number is  $n=1$ . All the results from STABLE are obtained with a spectrum of poloidal mode numbers in the range  $m_l=[-3, +7]$ .

The ideal MHD stability results are expressed through the ratio between the square of the growth rate of the instability  $-\omega^2$  and the poloidal Alfvén rate,

$$\omega_{qA}^2 = B_0^2/\mu_0\rho_0q_{\text{edge}}^2R_0^2, \quad (\text{B6})$$

where  $\rho_0$  is the plasma mass density (assumed uniform) and  $q_{\text{edge}}=1/\iota^{\text{edge}}$  is the safety factor at the plasma edge. The results of the compressible code STABLE have been validated against many free and fixed-boundary cases; Fig. 11 shows the result for  $\varepsilon=1/3$  and  $\kappa=2$ , in the absence of any ideal conducting shell ( $\Lambda \rightarrow \infty$ ). The comparison<sup>21</sup> with the ERATO<sup>4</sup> calculations for toroidal mode numbers  $n=1$  and 2 is quite accurate, being obtained with a very limited range of poloidal mode numbers ( $m_l \in [-3, 7]$ ) at low  $q_0$  ( $\leq 1$ ) while requiring a slightly more extended range ( $m_l \in [-5, 15]$ ) at higher  $q_0$  ( $> 1$ ). The results of the compressible STABLE code have been finally validated (Fig. 12) against the free-boundary stability results for the Solovév equilibrium with “approximate inverse aspect ratio”  $\varepsilon=1/6$  and elongation  $\kappa=1$ , in the presence of an ideal conducting shell surrounding the plasma at a normalized plasma-shell distance  $\Lambda=2$ . The comparison<sup>21</sup> with the Kerner<sup>31</sup> and PEST<sup>2</sup> codes calculations for toroidal mode number  $n=1$  is rather accurate, while being obtained with a very limited range of poloidal mode numbers ( $m_l \in [-3, 7]$ ). Also, the results of the new compressible code STABLECN have been validated against many free and fixed-boundary cases of the Solovév analytical MHD equilibria.

<sup>1</sup>R. Von Lüster and E. Martensen, *Z. Naturforsch. A* **15**, 706 (1960).

<sup>2</sup>R. C. Grimm, J. M. Greene, and J. L. Johnson, in *Methods in Computational Physics*, edited by J. Killeen (Academic, New York, 1976), Vol. 16, pp. 253–280.

<sup>3</sup>F. Troyon, L. C. Bernard, and R. Gruber, *Comput. Phys. Commun.* **19**, 161 (1980).

<sup>4</sup>R. Gruber, F. Troyon, D. Berger, L. C. Bernard, S. Rousset, R. Schreiber, W. Kerner, W. Schneider, and K. V. Roberts, *Comput. Phys. Commun.* **21**, 323 (1981).

<sup>5</sup>R. Gruber, S. Semenzato, F. Troyon, T. Tsunematsu, W. Kerner, P. Merkel, and W. Schneider, *Comput. Phys. Commun.* **24**, 363 (1981).

<sup>6</sup>C. Z. Cheng and M. S. Chance, *J. Comput. Phys.* **71**, 124 (1987).

<sup>7</sup>A. Ardelea and W. A. Cooper, *Phys. Plasmas* **4**, 3482 (1997).

<sup>8</sup>M. N. Rosenbluth and M. N. Bussac, *Nucl. Fusion* **19**, 489 (1979).

<sup>9</sup>M. Okabayashi and A. M. M. Todd, *Nucl. Fusion* **20**, 571 (1980).

<sup>10</sup>P. Gautier, R. Gruber, and F. Troyon *Nucl. Fusion* **21**, 1399 (1981).

<sup>11</sup>D. Brennan, P. K. Browning, R. A. M. Van der Linden, A. W. Hood, and

- S. Woodruff, Phys. Plasmas **6**, 4248 (1999).
- <sup>12</sup>M. S. Chance, Phys. Plasmas **4**, 2161 (1997).
- <sup>13</sup>J. Nührenberg and R. Zille, *Proceedings of the Workshop on Theory of Fusion Plasmas, EUR 11336 EN* (Editrice Compositori, Bologna, 1987), p. 3.
- <sup>14</sup>A. H. Boozer, Phys. Fluids **24**, 1999 (1981).
- <sup>15</sup>J. P. Freidberg, Rev. Mod. Phys. **54**, 801 (1982).
- <sup>16</sup>W. A. Cooper, Plasma Phys. Controlled Fusion **34**, 1011 (1992).
- <sup>17</sup>F. Alladio, A. Mancuso, P. Micozzi, and F. Rogier, Phys. Plasmas **12**, 112502 (2005).
- <sup>18</sup>A. Pletzer, A. Bondeson, and R. L. Dewar, J. Comput. Phys. **115**, 530 (1994).
- <sup>19</sup>R. Gruber and J. Rappaz, *Finite Element Methods in Linear Ideal Magnetohydrodynamics* (Springer-Verlag, Berlin, 1985), p. 39.
- <sup>20</sup>F. Alladio, A. Mancuso, P. Micozzi, and F. Rogier, Phys. Plasmas **13**, 082505 (2006).
- <sup>21</sup>M. S. Chance, J. M. Greene, R. C. Grimm, J. L. Johnson, J. Manickam, W. Kerner, D. Berger, L. C. Bernard, R. Gruber, and F. Troyon, J. Comput. Phys. **28**, 1 (1978).
- <sup>22</sup>L. S. Solovév, Sov. Phys. JETP **26**, 400 (1968).
- <sup>23</sup>J. Manickam, N. Pomphrey, A. Bondeson, and F. Paoletti, in *Proceedings of the 26th EPS Conference on Controlled Fusion and Plasma Physics, Maastricht* (ECA, 1999), Vol. 23J, p. 1657.
- <sup>24</sup>F. Rogier, G. Bracco, A. Mancuso, P. Micozzi, and F. Alladio, in *Proceedings of the 11th International Congress on Plasma Physics, ICPP 2002, Sydney, 2002*, edited by I. S. Falconer, R. L. Dewar, and J. Khachan (American Institute of Physics, Melville, NY, 2003), Vol. 669, p. 557.
- <sup>25</sup>J. B. Taylor and M. F. Turner, Nucl. Fusion **29**, 219 (1989).
- <sup>26</sup>X. Z. Tang and A. H. Boozer, Phys. Plasmas **13**, 042514 (2006).
- <sup>27</sup>F. Alladio, P. Costa, A. Mancuso, P. Micozzi, S. Papastergiou, and F. Rogier, Nucl. Fusion **46**, S613 (2006).
- <sup>28</sup>P. M. Morse and H. Feshbach, *Methods of Theoretical Physics* (McGraw-Hill, New York, 1953).
- <sup>29</sup>N. Amemiya, A. Morita, and M. Katsurai, J. Phys. Soc. Jpn. **63**, 1552 (1993).
- <sup>30</sup>J. R. Shewchuk, Comput. Geom. **22**, 21 (2002).
- <sup>31</sup>W. Kerner, Nucl. Fusion **16**, 643 (1976).